Coastal Engineering 189 (2024) 104457

Contents lists available at ScienceDirect

Coastal Engineering

journal homepage: www.elsevier.com/locate/coastaleng

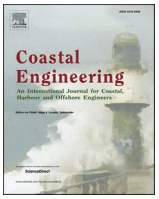

Experimental study of coherent structures and bed shear stress on a smooth bed under a solitary wave

Francis C.K. Ting *, Gunnar S. Kern

Department of Civil and Environmental Engineering, South Dakota State University, Brookings, SD, USA

ARTICLE INFO

Keywords:
Solitary wave
Coherent structures
Bed shear stress
Boundary layer
Bursting phenomenon
Law of the wall

ABSTRACT

The coherent structures induced by a solitary wave on a smooth bed were studied in a wave flume. The solitary wave was near the point of incipient breaking and the wave Reynolds number was in the intermittent turbulent regime. The velocity field inside the bottom boundary layer was measured using a Particle Image Velocimetry (PIV) system. The bed shear stress was obtained from the measured velocities in the viscous sublayer by employing the Newton's law of viscosity. It was found that the generation and maintenance of turbulent coherent structures in a solitary wave boundary layer was like that observed in oscillatory flow boundary layers at similar wave Reynolds numbers, a process that was first described as the bursting phenomenon in the wall boundary layer of steady flows. The effect of coherent structures on the instantaneous velocity profile and bed shear stress was examined. Ejections and sweeps were found to play a crucial role in producing large bed shear stress fluctuations. Quadrant analysis and probability distribution plots of the bed shear stress showed that sweep (Q_4) events were responsible for producing instantaneous bed shear stress values as high as four to five times the standard deviation above the mean, while ejection (Q_2) events produced bed shear stress values mostly below the mean. Both types of events were more numerous than outward interaction (Q_1) and inward interaction (Q_3). It was also found that a high proportion of the measured velocity profiles that did not follow the law of the wall were associated with large vortices in the boundary layer. It was shown that the instantaneous velocities did not conform to a law-of-the-wall velocity profile unless the measured velocity field was averaged over an area large compared to the vortices.

1. Introduction

The structure of the wave bottom boundary layer determines the fluid stresses exerted by surface waves on the seabed and the energy loss in wave propagation and thus is an important subject in nearshore hydrodynamics and sediment transport. The problem has been studied extensively for oscillatory flows in closed conduits, both experimentally and numerically because of the wide range of Reynolds numbers, from laminar to fully developed turbulent flows, that can be obtained in such facilities. Two recent reviews can be found in van der A et al. (2018) and Mier et al. (2021). The present study deals with coherent structures in the bottom boundary layer of a solitary wave, which is relatively unexplored. Although there is less applicability for this type of flow compared to regular waves, solitary waves are easier to reproduce in the laboratory because one would not have to be concerned with contamination from wave reflection and the subsequent buildup of low-frequency motion in the wave flume. Solitary waves also exhibit many of the same characteristics as regular waves but can be numerically reproduced with much less computational costs. This advantage makes solitary waves particularly important in boundary layer research because one can use finer computational grid resolution to develop wall-resolved models of coherent structures. After the models have been validated using experimental data, they can then be used to simulate wave conditions not reproducible in the laboratory.

In this study, the soliton propagates on a smooth, plane slope and is at the point of incipient breaking, so that the fluid motion is strongly acceleration skewed. The objective of the experimental investigation is to measure the instantaneous near-bed velocity profile and bed shear stress induced by the coherent structures and study their characteristics. Although fully rough, turbulent flow would normally be found in the bottom boundary layer under field conditions, studying the boundary layer flow over a smooth bed is important because one can then determine the bed shear stress directly from the measured velocities in the viscous sublayer without assuming the existence of a logarithmic layer,

* Corresponding author.
E-mail address: francis.ting@sdstate.edu (F.C.K. Ting).

https://doi.org/10.1016/j.coastaleng.2024.104457
Received 9 December 2022; Received in revised form 31 May 2023; Accepted 4 January 2024
Available online 13 January 2024
0378-3839/

which may or may not exist depending on the flow regime and wave phase. Therefore, studying the boundary layer flow on a smooth bed may serve as a "bridge" to understanding the structure of turbulent flow over a rough bed. Together with an on-going experimental investigation on the impact of breaking-wave-generated vortices on a plane slope, our overall goal is to understand the differences and similarities in the kinematics and dynamics of the bottom boundary layer in two related yet very different flow conditions, where in the case of the near-breaking wave coherent structures generated in the bottom boundary layer are the main source of turbulence in an otherwise irrotational flow, whereas in the post-breaking wave large breaking-wave-induced vortices are generated at the free surface then impinge on the bottom to disrupt the bottom boundary layer in a series of violent and episodic turbulent events. Selected publications relevant to the present study are reviewed herein.

Hino et al. (1983) measured the velocity profile of oscillatory flow in a wind tunnel using a laser-Doppler anemometer (LDA) and a hot-wire anemometer (HWA). Their experiment was conducted at a wave Reynolds number ($Re = aU_{0m}/\nu$) of 3.8×10^5, where a is half of the fluid particle oscillation excursion, U_{0m} is the amplitude of the free-stream velocity, and ν is the kinematic viscosity. Their measurements showed that turbulence is suppressed in the acceleration phases, but grows explosively at the beginning of flow deceleration, and then is reduced to a very low level at the end of the deceleration phases. By means of flow visualization, they observed that the abrupt generation of turbulence at the onset of flow deceleration was associated with the bursting phenomenon first described in the wall boundary layer of steady flows (e.g., Kline et al., 1967; Kim et al., 1971; Offen and Kline, 1974, 1975). Quadrant analysis further showed that the contribution to the phase-averaged Reynolds stress by "ejection" events is greater than the contribution by "sweep'' events, and that both types of events prevail over "inward interaction" and "outward interaction". It was also found that the logarithmic layer grows with time with the von Kármán constant κ and y-intercept in the log-law velocity profile approaching the universal values for steady flows of 0.4 and 5.5, respectively, at the later stage of flow deceleration.

Carstensen et al. (2010) conducted experiments with oscillatory flow and combined oscillatory flow and current in an oscillating water tunnel. They studied the characteristics of coherent structures in the wall boundary layer by means of flow visualization and measured the bed shear stress using a hot-film probe. The free-stream velocity was measured using a one-component LDA to provide phase information for the bed shear stress measurements. Their experiments covered a range of Reynolds numbers in the transitional flow regime. They observed two different kinds of coherent flow structures which they termed vortex tubes and turbulent spots. Vortex tubes were observed for wave Reynolds numbers in the range of 7×10^4 to 3×10^5. These are two-dimensional vortices that emerge after near-wall flow reversal and are caused by an inflectional-point instability in the laminar oscillatory flow velocity profile. They observed that the passage of these vortices produced a series of small fluctuations in the measured bed shear stress. In contrast, turbulent spots are violent oscillations or bursts in the boundary layer that mark the onset of turbulence. They are observed only for Reynolds numbers greater than 1.5×10^5. It was found that turbulent spots first appear during the deceleration phases but emerge earlier and earlier as the Reynolds number increases. It was also found that they caused high frequency, large fluctuations in the bed shear stress with peaks as high as 3 to 4 times the phase-averaged values.

Coherent structures in the wall boundary layer were investigated for solitary flow motion in an oscillating water tunnel by Sumer et al. (2010). In addition to flow visualization and hot-film probe measurements, the velocity profile was measured using a one-component LDA for determining the mean and turbulence characteristics of the streamwise velocity. Their experiments covered a wide range of Reynolds number from laminar to transitional flows up to $Re = 1.8 \times 10^6$, where Re is defined based on the maximum value of the free-stream velocity and half of the stroke of the water particle displacement in the free stream. They found that the flow is laminar for $Re < 2 \times 10^5$, laminar with vortex tubes for $2 \times 10^5 \leq Re \leq 5 \times 10^5$, and transitional with turbulent spots for $Re > 5 \times 10^5$. As in oscillatory flow boundary layers, the measured bed shear stress in the solitary flow boundary layer exhibits strong single or multiple spikes associated with turbulent spots, which first emerge towards the end of the flow period but gradually spread to earlier phases as the Reynolds number is increased. Unlike the experiment by Hino et al. (1983), their measured mean velocity profiles did not exhibit a well-defined logarithmic region, suggesting that the boundary layer was not in the fully developed turbulent regime even at the highest Reynolds number investigated in their experiments. Those results also indicate that the transition to turbulence is very sensitive to experimental conditions.

Numerical studies of coherent structures in oscillatory flow boundary layers on a smooth wall include Vittori and Verzicco (1998), Costamagna et al. (2003), Mazzuoli et al. (2011), Scandura et al. (2016) and van der A et al. (2018), among others. These models solve the continuity and Navier-Stokes equation by direct numerical simulation (DNS) with the no-slip condition at the wall, and thus avoid making any assumptions about the flow physics in the near-wall region. The numerical models were simplified by assuming that the mean flow was homogeneous in the streamwise and spanwise direction, and that the shear stress was vanishing far from the wall. The study by Costamagna et al. (2003) showed that in the transitional (intermittent turbulent) flow regime, low-speed streaks like those found in steady-flow boundary layers emerge at the end of the accelerating phases of the flow cycle, continue to grow during the early part of the decelerating phases, then break up into small-scale vortices. Analysis of the computed vorticity field revealed the existence of longitudinal vortices of alternating signs aligned with low-speed streaks pumping low-momentum fluid away from the wall. Mazzuoli et al. (2011) re-produced the turbulent spots observed in the experiment of Carstensen et al. (2010) by means of DNS. They showed that turbulent spots are associated with the breakup of low-speed streaks. Their numerical results also showed that the ensemble-averaged bed shear stress increases with the appearance of turbulent spots. In a related study, Vittori and Blondeaux (2008) modeled the turbulent boundary layer of a solitary wave with a free surface by DNS.

Most of the studies on oscillatory boundary layer flows are concerned with symmetric fluid motion. In acceleration-skewed oscillatory flows the free-stream velocity has a sawtooth-shaped time history. The free-stream velocity increases in magnitude faster during the acceleration phases. The associated boundary layer has a shorter time to form and consequently would develop a larger maximum bed shear stress. Scandura et al. (2016) conducted a numerical study of wall-bounded acceleration-skewed oscillatory flows by means of DNS, with special attention to the effect of coherent structures on the wall shear stress. Their numerical results showed that the breakup of low-speed streaks causes a large increase in the wall shear stress, with the relative intensity (ratio of root-mean-square of the fluctuations to the mean value) and skewness of the streamwise wall shear stress taking values of about 0.4 and 1.1, respectively. It was also found that the duration with large bed shear stress fluctuations increases with the wave Reynolds number, while the phase when this begins is dependent on both the wave Reynolds number and acceleration skewness. In a follow-up study, van der A et al. (2018) examined the higher-order statistics of turbulent velocity fluctuations in an asymmetric oscillatory boundary layer flow on a smooth wall using experimental data and the results of direct numerical simulations.

Experimental and numerical studies have shown that the breakup of low-speed streaks produces large bed shear stress fluctuations, and the phase of the onset of turbulence depends on the wave Reynolds number. Because of wall friction, the near-wall flow will start to decelerate before the flow in the free stream. Consequently, the wall shear stress has a

phase lead over the free-stream velocity. For oscillatory flows over a smooth bed, the phase lead is 45° for a laminar boundary layer and decreases to about 10° at $Re \approx 1 \times 10^6$ (Jensen et al., 1989). In transitional flows, the maximum bed shear stress occurs not in the acceleration phases, but with the generation of turbulent bursts during the deceleration of the flow (Hino et al., 1983; Jensen et al., 1989). The phase difference between the maximum bed shear stress and maximum free-stream velocity was investigated in an oscillating water tunnel by Mier et al. (2021). They measured the velocity profiles of oscillatory flows over a smooth wall using a three-component LDA for a range of wave Reynolds numbers from 3.2×10^4 to 8.6×10^5 covering the entire transitional flow regime. They determined the bed shear stress from the measured velocity gradient in the viscous sublayer. Their measurements showed that in the laminar regime, the phase-averaged bed shear stress has a single peak near the middle of the acceleration phases. With transition to turbulence, a second peak occurs near the middle of the deceleration phases, which becomes higher and occurs earlier as the Reynolds number is increased. They found that the "turbulent" peak is higher than the "laminar" peak at a Reynolds number of about 2.9×10^5. The "laminar" peak then disappears, and the "turbulent" peak develops a phase lead over the maximum free-stream velocity when the Reynolds number is greater than about 5×10^5. They also found that the logarithmic profile exists over a longer period as the Reynolds number increases.

The fluid motion in an oscillating water tunnel is different from that in a wave flume; the water particle velocity is one-dimensional and totally uniform. Boundary layer flow has been studied in wave flumes mainly at low to moderate Reynolds numbers. Liu et al. (2007) measured the laminar velocity profiles under solitary waves propagating on a smooth, horizontal bottom using PIV. They determined the bed shear stress by fitting a straight line to the measured velocity data close to the bed and employing the Newton's law of viscosity. Cox and Kobayashi (2000) measured the velocity distributions under shoaling and breaking regular waves on a 1:35 impermeable slope using a two-component LDA. Beach sand was glued to the fixed bed to create a fully rough, turbulent boundary layer. They found that in the bottom boundary layer outside the surf zone, fluctuations in turbulent kinetic energy and turbulent shear stress occur with the passage of each wave and are well described by their phase-averaged values, suggesting that turbulence production occurs at about the same phases in successive waves. Quadrant analysis of turbulent velocity fluctuations further showed that ejection and sweep events are more prevalent than inward and outward interactions. Sumer et al. (2011) used a hot-film probe to measure the bed shear stress induced by a solitary wave propagating on a 1:14 slope. The bottom boundary layer was in the transitional turbulent regime outside the surf zone. The measured bed shear stress time history showed no turbulence generation during the acceleration phases but exhibited large fluctuations in the deceleration phases. Seelam et al. (2011) measured the bed shear stresses induced by solitary waves on a smooth bed in the laminar and transitional flow regimes using a shear plate. The measured data were used to investigate the total bed shear stress, which included skin friction and the pressure gradient force acting on the edge of the shear plate. Pujara and Liu (2014) developed a shear plate sensor together with a methodology to correct for the pressure gradient force, which they then employed to obtain accurate measurements of bed shear stress in a laminar boundary layer under solitary waves. Lin and Huang (2002) used a one-component LDA to measure the laminar boundary layer flow on a smooth bed in the pre-breaking zone of shoaling regular waves. They showed that the profiles of the maximum onshore and offshore velocity components can be described by a universal similarity profile by using the maximum and minimum free-stream velocities as velocity scales and the Stokes boundary layer thickness as a length scale. Using PIV, Lin et al. (2015a, b) measured the laminar velocity profiles induced by a solitary wave propagating over a horizontal bottom and on a 1:10 slope in the pre-breaking zone of a solitary wave.

In this study, a large solitary wave was generated in a wave flume then propagated onto a 1:40 plane slope. The incident wave has a free-stream velocity close to 1 m/s and a horizontal water particle excursion of around 0.6 m, resulting in a wave Reynolds number of about 2.5×10^5. A PIV system was used to measure the velocity field over a smooth bed in the longitudinal-vertical plane near the point of incipient breaking. The bottom boundary layer was in the transitional regime, so that the flow was laminar during the acceleration phases, but turbulence grew explosively at the beginning of flow deceleration with the generation of turbulent coherent structures. The bed shear stress was determined by fitting a straight line to the measured velocities in the viscous sublayer. The whole (in a 2D plane) flow field measurements of water particle velocity allow us to examine the effects of coherent structures on the near-bed velocity profile and instantaneous bed shear stress, which was not possible in previous studies that employed single-point measurement techniques such as LDA and hot-film probe or shear plate.

The remainder of this paper is organized as follows. Experimental equipment and procedure are described in section 2. The results of data analysis are presented in section 3. The structure of the mean flow and ensemble-averaged characteristics of turbulence in the boundary layer are investigated first. Next, we study PIV measurements of coherent structures and compare them with those observed in the wall boundary layer of steady and oscillatory flows. To identify turbulent events that produce large instantaneous bed shear stresses, we divide the measured bed shear stress values into four quadrants (Q_1 to Q_4) based on the signs of the turbulent velocity components u' and v' in the viscous sublayer and buffer layer and study their probability distributions. We then examine the measured velocity profiles without ensemble averaging to determine how well the instantaneous velocity profile follows the law of the wall in the bottom bounbary layer of a near-breaking wave. Discussion and conclusions are given in section 4.

2. Experimental method

2.1. Experimental conditions

The experiment was conducted in a 25-m-long, 0.9-m-wide, and 0.75-m-deep tilting flume equipped with a programmable piston type wave generator. The experimental setup is shown in Fig. 1. A solitary wave was generated in a constant water depth of 0.4 m then

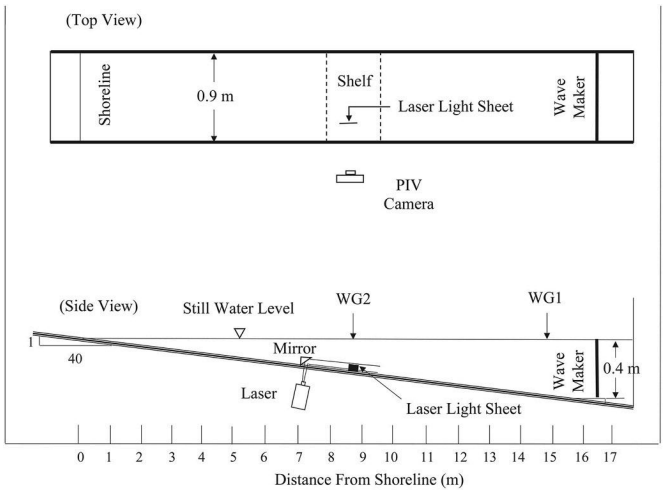

Fig. 1. Experimental arrangement. WG1 was located at a horizontal distance of 14.89 m and WG2 at 8.84 m from the still water shoreline. WG2 was positioned directly in front of the PIV camera. PIV measurements were conducted on a rectangular shelf 1.73 m long, 0.86 m wide and 27 mm high. The shelf is not shown in the side view.

immediately propagated onto a 1:40 plane slope. Wave elevations were measured sequentially at two locations, WG1 and WG2, on the plane slope using a resistance wave gage at a sampling rate of 50 Hz. WG1 was positioned at a still water depth of 0.369 m near the toe of the slope, while WG2 was positioned directly in front of the PIV camera where the still water depth was 0.187 m. The measured wave height at WG1 was 0.173 m. The horizontal water particle velocity, calculated as $\sqrt{gh}\bullet H/h$, was 0.892 m/s where g is acceleration of gravity, H is wave height, and h is still water depth. The horizontal water particle excursion, calculated as $\sqrt{16H/3h}\bullet h$, was 0.583 m (Goring, 1978). With a kinematic viscosity of 1.0533×10^{-6} m^2/s at a measured water temperature of 18°C, these results yield a wave Reynolds number Re, defined based on the maximum value of the free-stream velocity and half of the horizontal water particle excursion, of 2.5×10^5. Based on the oscillating water tunnel experiments by Sumer et al. (2010), the boundary layer of the incident solitary wave may be classified as in the transitional turbulent flow regime.

PIV measurements were conducted near the point of incipient breaking. The flume floor in the measurement area was covered by a checkerboard of 432 mm long × 432 mm wide porcelain tiles to create a smooth, rigid rectangular shelf 1.73 m long, 0.864 m wide and 0.027 m high. The installation of an elevated false bottom allowed optical access through the side wall down to the viscous sublayer for PIV measurements. The measured wave height and still water depth in front of the PIV camera were 0.211 m and 0.187 m, respectively, which yielded a H/h ratio of 1.12. The solitary wave curled over to form a plunging jet which hit the water onshore of the measurement area.

2.2. PIV system and setup

The PIV system used in this study was mostly the same as the Volumetric Three-Component Velocimetry (V3V) system used in Ting and Reimnitz (2015), except that one of the three PowerView Plus 4 MP cameras (2048 × 2048 pixels, 12-bit intensity dynamic range) was detached from the V3V camera probe and used for planar PIV measurement. Titanium dioxide particles (specific gravity 4.2, mean diameter 2 to 3 μm) were used as fluid tracers. The particle diameter was small enough to ensure adequate seeding in the wall region (viscous sublayer and buffer layer), which was only about 1 mm thick around the wave crest phase. The momentum response time of the tracer particles, calculated as $\rho_s D^2/(18\mu)$, where ρ_s and D are the density and mean diameter of the tracer particles and μ is the dynamic viscosity of water, is of the order of 10^{-6} s. This is much smaller than the characteristic time of the bursting process. The latter is comparable to the sampling interval of the PIV measurements (see below). The fall velocity of the tracer particles, calculated as $(\rho_s-\rho)gD^2/(18\mu)$, is of the order of 10^{-2} mm/s and is much smaller than the measured turbulent velocity fluctuations in a typical turbulence event. Therefore, the tracer particles would respond instantly to changes in the fluid velocity.

The PIV camera was positioned to view the flow field through the side wall of the flume. The laser (EverGreen double-pulse Nd-YAG system, 200 mJ/pulse) was mounted underneath the flume. A cylindrical lens (focal length −50 mm) and a focusing lens (focal length 1 000 mm) were mounted on the laser head to create a laser light sheet about 1 mm thick for planar illumination. The light sheet passed through the Plexiglass bottom onshore of the false bottom. A first surface mirror mounted on the flume floor re-directed the light sheet along the false bottom to illuminate the measurement area in front of the PIV camera (see Fig. 1). The distance between the laser light sheet and flume side wall was 169 mm. The angle of incidence of the light sheet was adjusted to minimize surface reflection from the false bottom, which was painted black. Calibration of the PIV camera was performed before the experiment by placing a calibration target in the laser light sheet plane. The calibration target had a rectangular grid of marker points with 5 mm spacing. An image of the calibration target was taken, and the calibration factor (15.27 μm/pixel) was determined by measuring the distance in pixels between the marker points.

A total of 26 experiment runs were carried out under the same incident wave condition. In each run, 30 straddled frames were captured at a repetition rate of 7.25 Hz, corresponding to 4 s of image capture when the solitary wave was passing in front of the PIV camera. Wave generation and image capture were triggered by a TTL signal generated by the data acquisition system. The timing of the trigger signal was adjusted so that the peak velocity at the wave crest phase was captured in the sequence of PIV images. The time interval between straddled frames was 200 μs. The PIV camera was fitted with a 105 mm/f2.8 Nikkor focal lens to capture the velocity field adjacent to the bottom. The field of view (FOV) was 27.4 mm long by 26 mm high parallel to the bottom. Post processing of PIV images was conducted by FFT correlation using the *INSIGHT 4G*^{TM} software by TSI. A background image was subtracted from each frame to increase the signal-to-noise ratio of the PIV images. The dimensions of the interrogation windows were 64 pixels by 16 pixels with a 50% overlap. The spatial resolution of the measured velocity field was 0.489 mm in the cross-shore direction and 0.122 mm in the "vertical" direction. A global range filter was used to remove spurious vectors, followed by vector validation using the local median. Missing vectors were replaced with neighborhood mean values, but no smoothing was applied. The percentage of interpolated vectors was between 5% and 10% over the entire PIV measurement area, and between 8% and 30% in the viscous sublayer and buffer layer. The number of spurious vectors was highest at the start of flow deceleration during the explosive growth of turbulence, but rapidly decreased thereafter. The validated velocity fields contained 57 vector columns in the cross-shore direction with 214 velocity points per column in the y-direction measured upward and perpendicular to the bottom.

The uncertainty in the PIV measurements was estimated as $\delta x/\delta t$, where δx is the uncertainty in the water particle displacement and δt is the time interval between straddled frames. PIV correlation peak displacement may be assumed to be accurate to within 1/10th of a pixel (Kiger, 2015). With the spatial resolution equal to 15.27 μm/pixel and δt equal to 200 μs, the measured velocities were resolvable to 8 mm/s. The latter is much smaller than the mean velocity in the cross-shore direction measured at the closest distance from the bed at the wave crest phase. The measurement uncertainties of the individual velocity components δu and δv were also evaluated by measuring the water particle velocities in quiescent water (Raffel et al., 1998). After seeding was added to the flume, the water was left undisturbed for 15 min then 40 PIV velocity fields were captured. The standard deviation of the measured velocities was 3 mm/s in the cross-shore direction and 2 mm/s in the vertical direction, which were deemed to be satisfactory.

2.3. Data analysis

The measured velocity field (u,v) was separated into an organized wave-induced component $(\widetilde{u},\widetilde{v})$ and a turbulence component (u',v') by the method of ensemble averaging, where the total number of trials was 20 (tests 7 to 26). The first six tests (1–6) were used to adjust the seeding density of the water, but the measured velocities were not used for data analysis. The turbulence intensity (u'^2,v'^2) and Reynolds stress $u'v'$, and their ensemble averages $(\widetilde{u'^2},\widetilde{v'^2})$ and $\widetilde{u'v'}$ were then computed. The repeatability of wave generation was very good. This had been demonstrated in Ting (2006). The uncertainty in the turbulence velocities was due to the uncertainty in PIV measurements and pseudo turbulence introduced by ensemble average subtraction. The total uncertainty was evaluated by examining the turbulence intensities outside the bottom boundary layer, which should be small under the non-breaking wave. The values of $\sqrt{<\widetilde{u'^2}>}$ and $\sqrt{<\widetilde{v'^2}>}$, where $<\ >$ is used to denote a FOV average (see below), in the free stream are around 6 mm/s and 4 mm/s, respectively. The uncertainties in u' and v' were

subtracted from the profiles of $\sqrt{<\widetilde{u'^2}>}$ and $<\sqrt{<\widetilde{v'^2}>}$ in Fig. 4 to better represent the turbulence intensities in the boundary layer.

Two types of spatial averaging were performed in data analysis. In FOV averaging, a flow quantity (e.g., $\widetilde{u}$) was averaged over 55 vector columns (columns 2 to 56, omitting the first and last columns) to produce a single profile representing the FOV-averaged velocity profile over the entire measurement area. In local averaging, the spatial averaging was performed over 5 neighboring columns (columns 2 to 6, 7 to 11, …., 52 to 56) to produce 11 profiles representing the local average over a bottom area approximately 2 mm long in the cross-shore direction and 1 mm wide (thickness of the laser light sheet) in the transverse direction. The diameter of a typical vortex generated by the bursting process in the experiment was around 6 mm. Therefore, the bed shear stress induced by the individual vortices was adequately resolved by the local average velocity profiles. In this paper, an accent ($\sim$) placed over a flow quantity (e.g., $\widetilde{u}$) is used to represent an ensemble average, and the operator ($<\ >$) denotes taking the spatial average over the entire FOV. For example, the FOV- and ensemble-averaged velocity in the cross-shore direction is denoted by $<\widetilde{u}>$. Local averaging, where performed, will be indicated in the text. Note that spatial averaging can be performed on the measured fluid velocities with or without ensemble averaging; this will be discussed.

Bed shear stress was determined by fitting a straight line to the measured velocity points in the viscous sublayer, defined as $y^+ \lesssim 10$ where $y^+ = yu^*/\nu$ is the height of the measurement point above the smooth bed in wall units, u^* is the friction velocity, and ν is the kinematic viscosity. There were only 2 or 3 velocity points that satisfied this criterion around the wave crest phase. Therefore, the 95% confidence intervals of the bed shear stress estimates were large. Nevertheless, bed shear stress measurements of turbulent coherent structures in wave bottom boundary layers are scarce. Therefore, the measured data are a valuable addition to the existing database. Note that the bottom was not used as a data point in the linear fit. Its location was determined by the y-intercept to define the origin of the y coordinate and used as a check for the quality of the measured velocities in the viscous sublayer (see section 3.1). Due to reflection of the laser light sheet, the bottom boundary had a line thickness of 2–3 pixels in the PIV images. Since the vertical spacing between the velocity points was only 8 pixels, a significant systematic error could result if the location of the bottom was misplaced by just 1 or 2 pixels. Note that when the instantaneous bed shear stress induced by a vortex is sought, the measured velocity profiles from the different experiment runs are not ensemble averaged. Instead, local averaging is performed on the measured velocity profiles then the local bed shear stress is found by fitting a straight line to the "average" velocities in the viscous sublayer. Local averaging smooths out noise in the measured data thereby reducing the measurement uncertainty in the bed shear stress.

3. Experimental results

3.1. Ensemble-averaged properties of the flow field

Fig. 2 shows the variation of the FOV- and ensemble-averaged velocity profile with time under the solitary wave. The spatial averaging was performed over columns 2 through 55. The complete time series contains 30 wave phases sampled at 7.25 Hz. A nondimensionalized time is defined as $t' = t\sqrt{g/h}$, where t is time, h is the still water depth in the measurement area ($= 0.187$ m), and $t = 0$ is taken as the instant of the maximum free-stream velocity. The measured velocity profiles are presented from $t' = -3$ to 12. To avoid cluttering, only 1 out of every 5 velocity points are plotted after the first 10 data points above the bed. The smooth bed is located at $y = 0$. A maximum free-stream velocity of 0.99 m/s is measured at $t' = 0$. The near-bed flow reverses direction after $t' = 8$ and moves in opposite direction to the flow in the free stream. Note the indentation in the velocity profile just outside the wall region at $t' = 0$. It was caused by the sudden growth of turbulence at this phase. The lifting of low-speed fluid from the bed created an inflection in the measured velocity profiles and the formation of large transverse

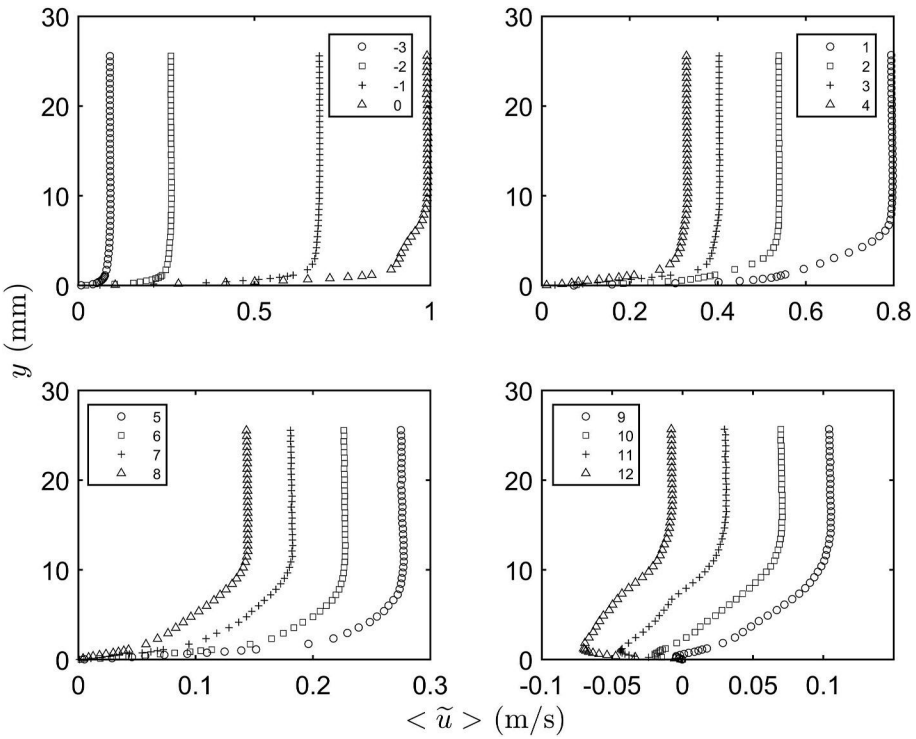

Fig. 2. Profiles of FOV- and ensemble-averaged velocity in the cross-shore direction at different phases of the solitary wave. The wave crest phase is at $t' = 0$. Flow reversal at the bed occurs at $t' = 8$. Only 1 out of every 5 velocity points is plotted after the first 10 data points above the bed.

vortices (see section 3.2), and since these events occurred every time at the beginning of flow deceleration, the ensemble-averaged (mean) velocity also develops an inflectional profile. The mean velocity profile returns to the normal shape after the breakup of the vortices; this will be discussed.

After the abrupt growth of turbulence at $t^{'} = 0$ and 1, the turbulence intensity decreases temporarily at $t^{'} = 2$ and 3, then increases again. The generation of coherent structures in this second period was more irregular. Consequently, the ensemble-averaged velocity does not display an inflectional profile. After $t^{'} = 8$, a shear layer developed between the reversed flow adjacent to the bed and the shoreward flow away from the bed. Shear instabilities led to the formation of Kelvin-Helmholtz (KH) vortices. Defining the top of the boundary layer as the position where the velocity magnitude reaches 99% of the free-stream value, the thickness of the boundary layer δ increases rapidly from 4.9 mm at $t^{'} = -1$ to 8 mm at $t^{'} = 0$, decreases slightly at $t^{'} = 1$ and 2, then increases again during the second period of turbulence generation to 10.7 mm before near-bed flow reversal at $t^{'} = 8$. From $t^{'} = 8$ to 12, the value of δ increases by another 5.3 mm due to mixing by the Kelvin-Helmholtz vortices.

Fig. 3 shows, from top to bottom, the variations of the non-dimensionalized wave elevation η/H, free-stream velocity U_0/U_{0m}, bed shear stress τ_b/τ_{bm}, and longitudinal pressure gradient $(-\partial p/\partial x)/(\rho g)$ in the free stream with time, where H is the wave height, and U_{0m} and τ_{bm} are the maximum free-stream velocity and bed shear stress measured at the wave crest phase, respectively. The wave elevation is the measured data from WG2. The free-stream velocity is found from the FOV- and ensemble-averaged velocity profiles shown in Fig. 2 by averaging the velocity data outside the boundary layer. The bed shear stress is obtained by fitting a straight line to the FOV- and ensemble-averaged velocity profile in the viscous sublayer. Free-stream velocity and bed shear stress values between the measured data points are then interpolated by spline fitting. The cross-shore pressure gradient is determined from the ensemble-averaged velocity field by employing the Reynolds-Averaged Navier-Stokes (RANS) equation:

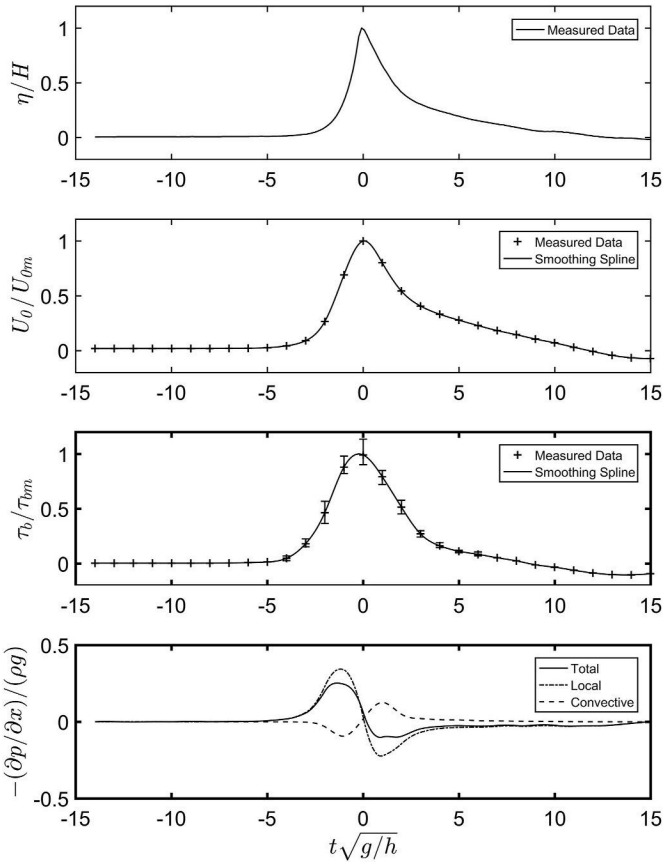

Fig. 3. Time histories of nondimensionalized water surface elevation, free-stream velocity, bed shear stress and pressure gradient in the cross-shore direction under the solitary wave; H = wave height, U_{0m} = magnitude of the FOV- and ensemble-averaged velocity in the free stream; τ_{bm} = maximum bed shear stress.

$$-\frac{\partial \widetilde{p}}{\partial x} = \rho\left(\frac{\partial \widetilde{u}}{\partial t} + \widetilde{u}\frac{\partial \widetilde{u}}{\partial x} + \widetilde{v}\frac{\partial \widetilde{u}}{\partial y}\right) + \rho\left(\frac{\partial \widetilde{u^{'}u^{'}}}{\partial x} + \frac{\partial \widetilde{u^{'}v^{'}}}{\partial y}\right) - \mu\left(\frac{\partial^2 \widetilde{u}}{\partial x^2} + \frac{\partial^2 \widetilde{u}}{\partial y^2}\right) \quad (1)$$

where ρ is fluid density and μ is dynamic viscosity. In Eq. (1), $\partial\widetilde{u}/\partial t$ is the time derivative of the free-stream velocity obtained by spline fitting as shown in the second plot of Fig. 3. The spatial derivatives are computed frame by frame from the distributions of the ensemble-averaged velocities $\widetilde{u}$ and $\widetilde{v}$ and turbulence stresses $\widetilde{u^{'}u^{'}}$ and $\widetilde{u^{'}v^{'}}$. The results are averaged over the FOV, and time series are constructed by spline fitting like the average free-stream velocity and bed shear stress.

In addition to the mean bed shear stress determined from the FOV- and ensemble-averaged velocity profile, the plot for τ_b/τ_{bm} includes the range of bed shear stress values obtained from 11 local average, ensemble-averaged velocity profiles (see section 2.3). At the wave crest phase ($t^{'} = 0$), the local average, ensemble-averaged bed shear stress ranges from 1.4 to 1.8 N/m^2, with a mean value of 1.55 N/m^2. The latter is virtually identical to the bed shear stress determined from the FOV- and ensemble-averaged velocity profile. As a check, we compute the maximum bed shear stress induced by solitary flow motion in oscillating water tunnel using the friction factor diagram developed by Sumer et al. (2010). For a wave Reynolds number of 2.5×10^5, the friction factor f is between 0.0025 and 0.003 (see Fig. 15a in their paper). With $\rho = 998.57$ kg/m^3 and $U_{0m} = 0.99$ m/s, we obtain a value for $\tau_{bm}(= \rho f U_{0m}{}^2/2)$ between 1.2 and 1.5 N/m^2. Since the bed shear stress should be greater under a solitary wave that is acceleration-skewed, our measured values are consistent with their experimental results.

A maximum wave-induced cross-shore pressure gradient $-(\partial p/\partial x)/\rho g$ of 0.252 mH$_2$0/m is found in the free stream at $t^{'} = -1.3$ under the front face of the solitary wave. The pressure gradient drops to nearly zero at $t^{'} = 0$. The adverse pressure gradient during flow deceleration is much smaller, with a minimum value of about -0.1 mH$_2$0/m at $t^{'} = 0.86$. Note that both local and convective accelerations contribute significantly to the total fluid acceleration. These results are consistent with published data (e.g., Baldock, 2012).

With the local and convective fluid accelerations thus determined, we can calculate the acceleration-skewness parameter defined as (van der A et al., 2011):

$$\beta = \frac{a_{0\ max}}{a_{0\ max} - a_{0\ min}} \quad (2)$$

where $a_{0\ max}$ and $a_{0\ min}$ are the maximum and minimum accelerations of the water particles in the free stream. The computed value of β is 0.72, compared to 0.5 for sinusoidal waves. Thus, the solitary wave motion is strongly acceleration skewed.

Fig. 4 presents the profiles of the turbulence stresses $\sqrt{<\widetilde{u^{'2}}>}/u^*$, $\sqrt{<\widetilde{v^{'2}}>}/u^*$ and $-<\widetilde{u^{'}v^{'}}>/u^{*2}$ normalized by the friction velocity $u^*(=\sqrt{\tau_b/\rho})$ and plotted against $y^+(=yu^*/\nu)$. The plots are organized into three different time periods. The first period, which lasts from $t^{'} = -1$ to 3, has the largest measured bed shear stress and is the focus of this study. The boundary layer was not turbulent until the end of the acceleration phases when turbulence started to appear next to the bed at $t^{'} = -1$. With the beginning of flow deceleration, turbulence grew explosively at $t^{'} = 0$ (top plot) and spread rapidly upwards. The

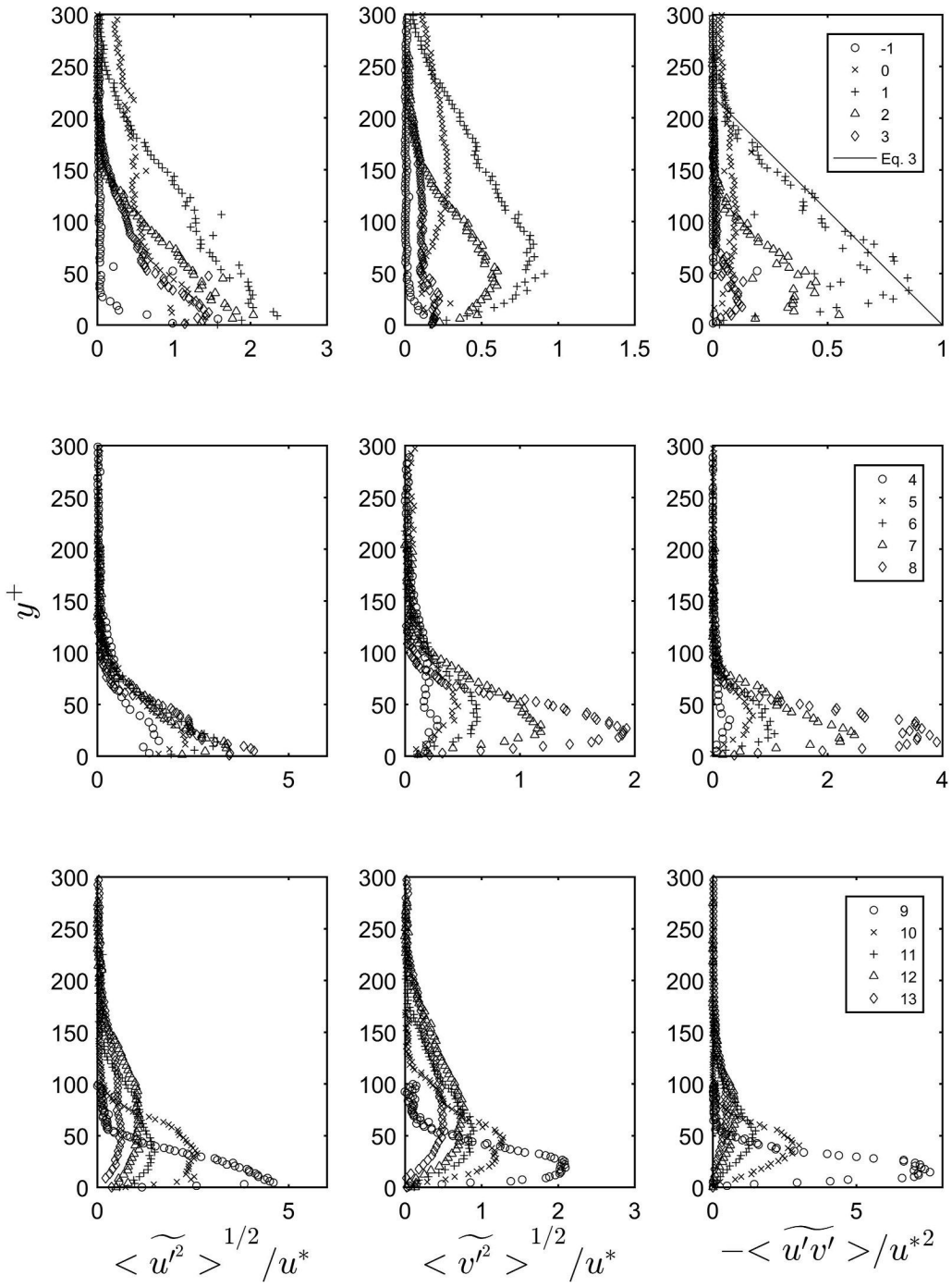

Fig. 4. Profiles of nondimensionalized turbulence stresses $\sqrt{< \widetilde{u'^2} >}/u^*$, $\sqrt{< \widetilde{v'^2} >}/u^*$ and $- < \widetilde{u'v'} > /u^{*2}$ at different phases under the solitary wave. To avoid cluttering, only 1 out of every 3 data points are plotted from $t' = 4$ to 13.

normalized root-mean-square (r.m.s.) u' increases until $t' = 1$ when a maximum value of 2.35 is measured at $y^+ = 8.6$. The peak value of $\sqrt{< \widetilde{u'^2} >}/u^*$ is close to the value of 2.3 often cited for steady open-channel flow (see Nezu and Nakagawa, 1993). Fig. 5 shows a raw PIV image from $t' = 0$. It was obtained by overseeding the measurement area then allowing the seeding particles to settle before generating the solitary wave. The image shows that turbulence production is characterized by the lifting of streaky structures from the bed and formation of large transverse vortices. These periodic vortices are reminiscent of the hairpin vortices observed in a laminar boundary layer in the steady flow experiment of Acarlar and Smith (1987). To overcome the difficulty of detecting hairpin vortices that were quasi-periodic in space and time, they injected fluids slowly through a slot on the smooth bottom of a water channel to form an artificial low-speed region very near the wall to mimic the low-speed streaks in the bursting process. The periodic vortices shown in Fig. 5 closely resemble the roll-up of the shear layer formed by the lifting of low-speed streaks seen in their experiment. The distance from the bed to the top of the largest vortex in Fig. 5 is about $150\nu/u^*$, and the edge of the boundary layer is located at $y^+ \approx 220$. The periodic vortices left the measurement area after $t' = 0$ therefore their breakup could not be observed.

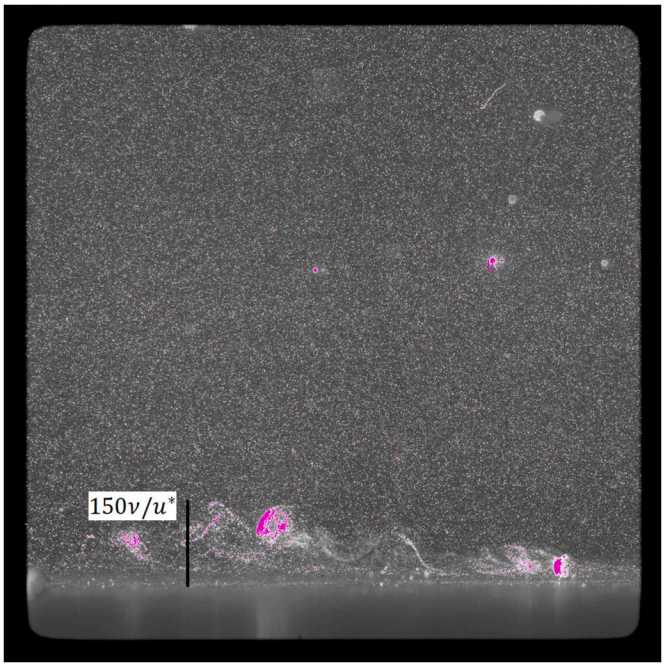

Fig. 5. Raw PIV image showing the lifting of low-speed streaks and formation of hairpin vortices. The black vertical bar shows the vertical distance measured in wall units.

Referring again to Fig. 4, the normalized r.m.s. u' decreases at $t' = 2$ and 3 with the breakup of the vortices but increases again afterwards (middle plot). The temporary re-laminarization of the flow may be expected for a transitional turbulent boundary layer. A second period of turbulence production occurs from $t' = 4$ to 8. It was caused by an adverse pressure gradient in a near-bed flow that was close to flow reversal (Jensen et al., 1989). Although the turbulence intensities are lower in the second period, the peak normalized r.m.s. u' value is higher because the bed shear stress becomes very small before near-bed flow reversal. The same behavior can be seen in oscillatory boundary layer flows over a smooth bed in the oscillating water tunnel experiment of Jensen et al. (1989). After near-bed flow reversal, the velocity profile developed an inflection point at some distance above the bed (see Fig. 2). Shear instabilities led to the formation of Kelvin-Helmholtz (KH) vortices, which were slowly advected offshore and decayed. As more of the boundary layer flow away from the bed reversed direction, Fig. 4 shows that the peak of the r.m.s. u' profile migrates upwards. At the same time, shear-induced mixing causes the r.m.s. profile for u' to become more uniform with time (bottom plot).

The trend of the normalized r.m.s. profiles for v' is like that for u'. In the top plot, the r.m.s. values of v' increase abruptly at $t' = 0$ due to the generation of the periodic vortices (see Fig. 5), with a maximum value of $\sqrt{<\widetilde{v'^2}>}/u^*$ equal to 0.28 measured at $y^+ \approx 140$. The bottom-generated turbulence continues to spread upwards from $t' = 0$ to $t' = 1$ when $\sqrt{<\widetilde{v'^2}>}/u^*$ attains a maximum value of 0.91 at $y^+ = 49.5$. The latter is somewhat smaller than the peak value of around 1.0 measured by Grass (1971) and 1.27 cited in Nezu and Nakagawa (1993) for steady open-channel flows. Compared to oscillatory flows, the peak value of $\sqrt{<\widetilde{v'^2}>}/u^*$ under the solitary wave is close to the value of about 0.9 measured by Hino et al. (1983) at a wave Reynolds number of 3.8×10^5, but is smaller than the value of about 1.0 obtained by Jensen et al. (1989) at a higher wave Reynolds number of 1.6×10^6 (see Fig. 22 in their paper). Note that a direct comparison with previous studies is difficult because the peak value of $\sqrt{<\widetilde{v'^2}>}/u^*$ varies with phase (see also Mier et al., 2021) and the period of turbulence production under the solitary wave was very short. As expected, the peak values of $\sqrt{<\widetilde{v'^2}>}$ are smaller than the peak values of $\sqrt{<\widetilde{u'^2}>}$. Another noticeable difference between the r.m.s. profiles for u' and v' in Fig. 4 is that the peak $\sqrt{<\widetilde{u'^2}>}$ values occur close to the bed while the peak $\sqrt{<\widetilde{v'^2}>}$ values occur farther away from the bed. This has also been observed in the wall boundary layer of steady flows (e.g., Grass, 1971; Nezu, 1977) and oscillatory flows (e.g., Jensen et al., 1989; van der A et al., 2011). The normalized r.m.s. v' increases from $t' = 4$ to $t' = 8$ in the second period (middle plot), before decreasing monotonically from $t' = 9$ to $t' = 13$ after flow reversal at the bed (lower plot).

The right plots in Fig. 4 show the Reynolds stress profiles normalized by the friction velocity. In steady, uniform open-channel flows the total shear stress, which includes the viscous shear stress and Reynolds stress, varies linearly from the bed shear stress to zero at the free surface as follows (Nezu and Nakagawa, 1993):

$$-\overline{u'v'} + \mu\frac{\partial \overline{u}}{\partial y} = u^{*2}\left(1 - \frac{y}{h}\right) \tag{3}$$

where h is the flow depth and the overbar denotes time averaging. Since the viscous shear stress is negligible outside the viscous sublayer and buffer layer, the bed shear stress $\tau_b (= \rho u^{*2})$ may be found by linearly extrapolating the measured Reynolds stress distribution in the outer layer to the bed. The dimensionless form of Eq. (3) $(= 1 - y/h)$ is included in the top plot with h taken as the thickness of the bottom boundary layer (=6.6 mm) at $t' = 1$. Eq. (3) fits the measured Reynolds stress distribution outside the wall region well at $t' = 1$. For the near-breaking wave, local and convective accelerations both played an important role in the momentum balance (see Fig. 3). Furthermore, the buildup of turbulence occurred over only a brief time from $t' = -1$ to 1. As seen in the top plot, the peak values of $<\widetilde{u'v'}>/u^{*2}$ are all much less than 1 except at $t' = 1$.

Fig. 6 shows the distribution of the correlation coefficient $R_{u'v'} = <-\widetilde{u'v'}>/\left(<\widetilde{u'^2}>^{1/2}<\widetilde{v'^2}>^{1/2}\right)$ from $t' = -1$ to 2. In steady, open-channel flows, the value of $R_{u'v'}$ increases with y/h in the wall region then remains nearly constant at 0.4–0.5 over much of the water column, before decreasing in the free surface region (Nezu and Nakagawa, 1993). Under the solitary wave, the correlation coefficient increases abruptly with the sudden generation of turbulence at the start of flow deceleration. At $t' = 0$, the value of $R_{u'v'}$ increases with distance above the bed and attains a maximum value between 0.4 and 0.5 around $y^+ = 70$, before decreasing slowly with the turbulence intensity in the outer layer (see the r.m.s. profiles for u' and v' in Fig. 4). At $t' = 1$, the value of $R_{u'v'}$ has decreased above $y^+ \approx 200$ due to the decay of turbulence away from the bed; and at $t' = 2$, the correlation between u' and v' has greatly diminished above $y^+ \approx 100$. Jensen et al. (1989) obtained a lower correlation coefficient of 0.2–0.3 in oscillatory boundary layer flows, which they attributed to the high drop-out rates near the wall in their LDA measurements. They suggested that this might be the cause for the discrepancy between the measured Reynolds stress and the bed shear stress obtained from their hot-film probe. In this present study, there is good correlation between u' and v' in the near-wall region. Therefore, the discrepancy between the measured Reynolds stress and bed shear stress may not be attributed to underestimating the Reynolds stress. Rather, it was an actual phenomenon related to the transient nature of turbulence production in a transitional turbulent boundary layer.

Fig. 7 shows, from top to bottom, profiles of the nondimensionalized mean velocity, mean velocity gradient, Reynolds stress, and turbulence

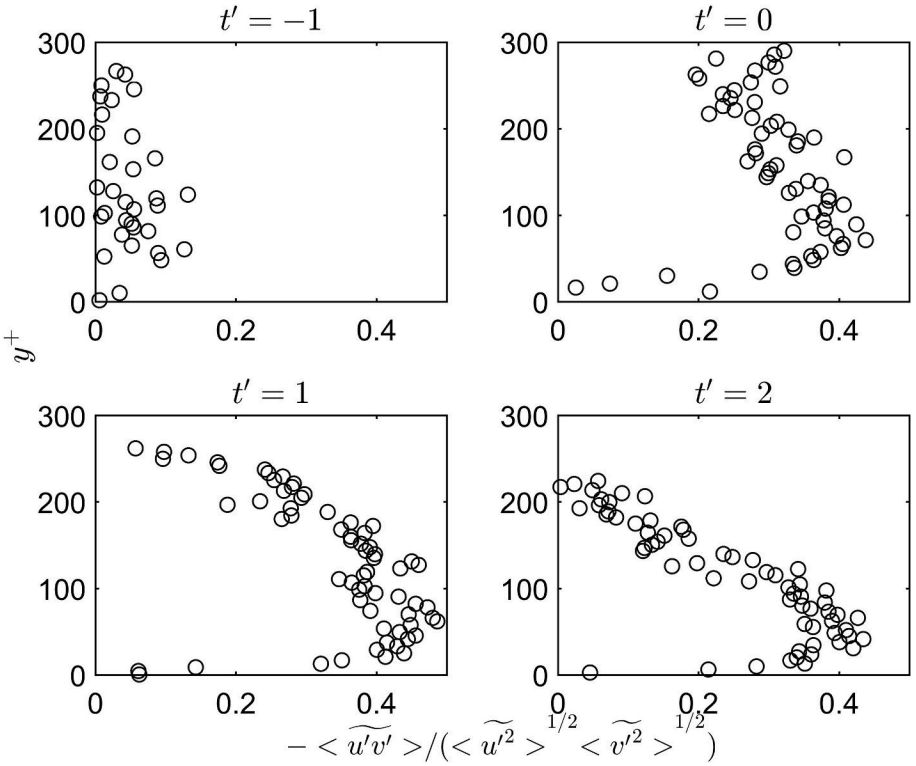

Fig. 6. Profiles of correlation coefficient $R_{\widetilde{u'v'}} = <-\widetilde{u'v'}> / \left(<\widetilde{u'^2}>^{1/2} <\widetilde{v'^2}>^{1/2} \right)$ from $t' = -1$ to 2.

production rate in the near-wall region at $t' = 1$. The plot for $<\widetilde{u}>$ shows only two velocity points in the region $y^+ < 10$. A straight line was fit to these two data points to estimate the bed shear stress τ_b $(= \rho u^{*2})$ and location of the smooth bed $(y = 0)$. A third data point closer to the bed (not shown) was not used for the linear fit because it would produce a y-intercept value outside the 2 to 3 pixels region where the smooth bed was expected to lie. As explained in section 2.3, the approximate location of the bottom was not used as a data point in the velocity profile fit. Instead, it was used to remove outliers and spurious vectors when determining the bed shear stress.

The values of $\partial <\widetilde{u}> / \partial y$ in the second plot were obtained by fitting a spline curve to the measured values of $<\widetilde{u}>$ shown in the top plot then computing the spatial derivative. The smoothing spline interpolation produces a slightly different result for $\partial <\widetilde{u}> / \partial y$ from a linear fit to the near-wall points, but the value of $(\nu / u^{*2})(\partial <\widetilde{u}> / \partial y)$ is close to 1 in the region $y^+ < 10$. The plot for $<\widetilde{u'v'}> / u^{*2}$ is the same plot shown in Fig. 4 but includes only the near-wall points with the outliers removed. It shows that the Reynolds stress remains constant from $y^+ \approx 30$ to 60 just outside the buffer layer, and that the maximum value of the Reynolds stress is close to the bed shear stress at $t' = 1$ as we have already discussed. In the bottom plot, a maximum value for $-(\nu / u^{*4}) < \widetilde{u'v'} > (\partial <\widetilde{u}> / \partial y)$ of 0.22 is found at $y^+ = 12.7$. These results are in good agreement with the theoretical values of 0.25 and 12, respectively, for steady turbulent flows in pipes (see Tennekes and Lumley, 1989). The bottom plot shows that most of the turbulence production occurs in the buffer layer $(5 < y^+ < 30)$. Similar results were found at $t' = 0$, 2 and 3 (not shown).

Fig. 8 presents semi log plots of the space- and ensemble-averaged velocity profile from $t' = 0$ to 3 in wall units. The spatial averaging was performed from columns 22 to 26 (transect 4 in Fig. 10a), but similar results were found at other locations. The universal logarithmic law for steady flow on a smooth bed is given by:

$$\frac{u}{u^*} = A \ln \frac{y u^*}{\nu} + B \tag{4}$$

where $A \approx 2.5$ and $B \approx 5.0$ (Tennekes and Lumley, 1989). Previous studies (e.g., Hino et al., 1983; Akhavan et al., 1991; Mier et al., 2021) have found that the value of B changes for different phases in oscillatory flows. With $A = 2.5$ and u^* determined from the velocity data in the viscous sublayer, the value of B was determined by fitting Eq. (4) to the local average and ensemble-averaged velocities in a semi log plot of $u^+ (= u / u^*)$ versus $y^+ (= y u^* / \nu)$. The wave Reynolds number of the solitary wave was not large enough for the boundary layer to remain fully turbulent except for a brief time. As seen in Fig. 8, a logarithmic region exists under the solitary wave only at $t' = 1$ and 2.

Also plotted in Fig. 8 is the Spalding wall function (Spalding, 1961):

$$y^+ = u^+ + 0.1108 \left[e^{0.4u^+} - 1 - 0.4u^+ - \frac{(0.4u^+)^2}{2!} - \frac{(0.4u^+)^3}{3!} - \frac{(0.4u^+)^4}{4!} \right] \tag{5}$$

Eq. (5) predicts the local average and ensemble-averaged velocity profile at $t' = 2$ well. Although only the velocity profile at transect 4 is shown, similar results were found at other locations in the measured velocity field; the values of B at the 11 transects range from 4.1 to 5.8. These results show that Eq. (5), with a linear velocity profile $(u^+ = y^+)$ when y^+ is small, the logarithmic distribution given by Eq. (4) when y^+ is large, and a buffer layer at the intermediate values of y^+, is fully displayed by the mean velocities only when the boundary layer approaches fully turbulent condition. The value of B is greater than 5.0 when the logarithmic layer is first detected at $t' = 1$ but approaches the universal value of 5.0 for steady turbulent boundary layer flows at $t' = 2$. The same trend was also found in the numerical results for acceleration-skewed oscillatory flows by Scandura et al. (2016).

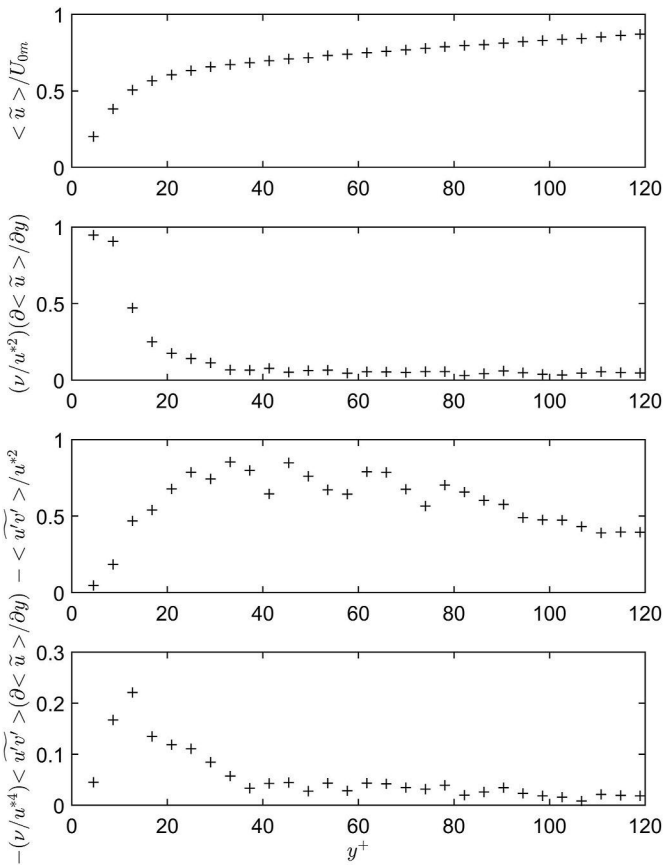

Fig. 7. Profiles of nondimensionalized FOV- and ensemble-averaged velocity in the cross-shore direction, viscous shear stress, Reynolds stress, and rate of turbulence production at $t' = 1.$ U_{0m} is the magnitude of the FOV- and ensemble-averaged velocity in the free stream.

3.2. Velocity fields of coherent structures

The solitary wave boundary layer was laminar during the acceleration phases. PIV measurements showed that at the start of flow deceleration, thin, elongated regions of low velocity fluid (low-speed streaks) began to appear next to the bed. The low-speed streaks lifted from the bed and rolled up to form one or more transverse vortices. High-speed fluid then rushed towards the bed in front or behind the transverse vortices. The phenomenon is reminiscent of the bursting process first observed in the wall boundary layer of steady flows. The term is used in the literature to denote a complete sequence of events that include streak lift-up, oscillation, ejection, and sweep (Nezu and Nakagawa,

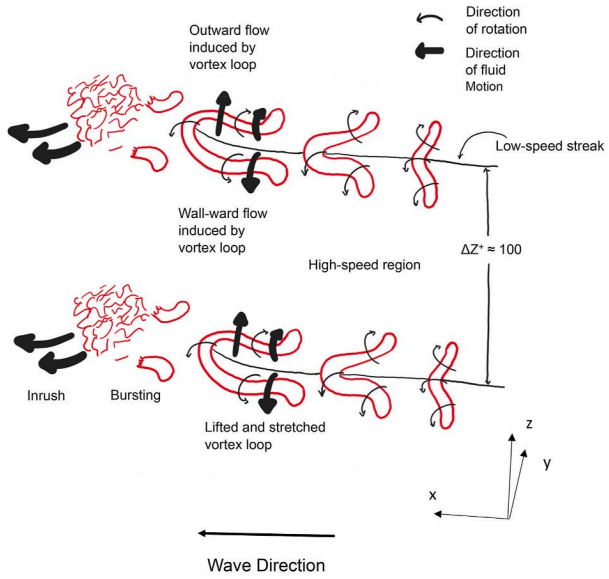

Fig. 9. Schematic of the bursting process.

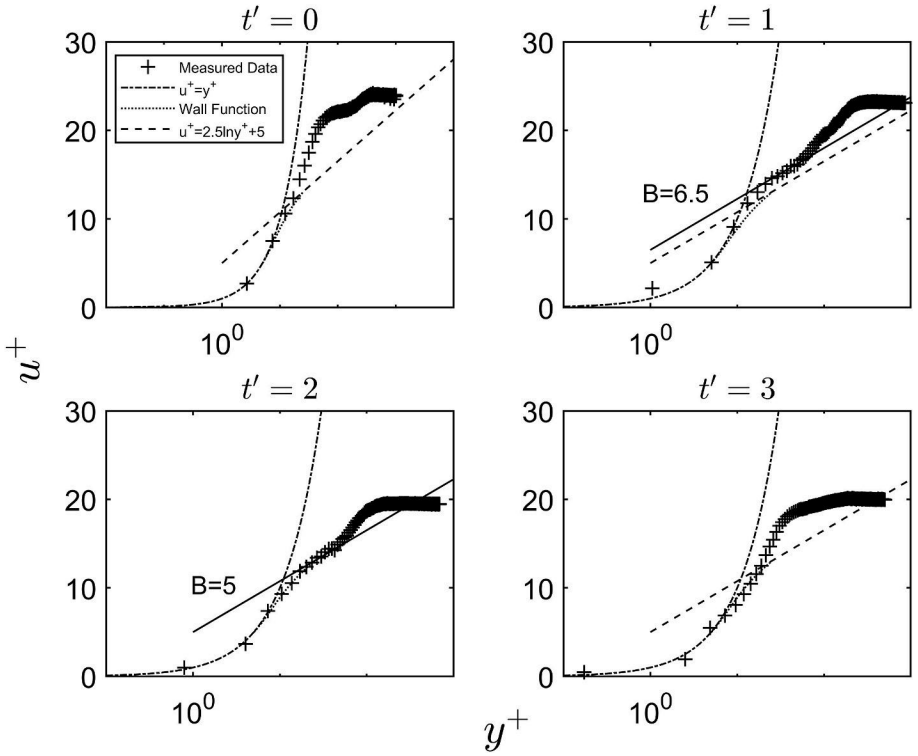

Fig. 8. Semi log plots of ensemble-averaged velocity profile in the cross-shore direction from $t' = 0$ to 3, transect 4.

1993). Fig. 9 shows a schematic of the bursting process like that depicted in Allen (1997). It is included here to aid the discussion of PIV measurements presented in this section. The basic model, as described in Kim et al. (1971) and Offen and Kline (1975), features the formation of a stretched and lifted horseshoe vortex loop following the lift-up of a low-speed streak and the development of an inflection point in the near-wall velocity profile. More information on the bursting process can be found in the review papers by Robinson (1991), Smith (1996), and Panton (2001), and in the monograph by Nezu and Nakagawa (1993). Smith (1984) proposed a refined model for the formation and breakup of hairpin vortices, which also includes a process for low-speed streak regeneration.

Fig. 10a shows the measured turbulent velocity field (u', v') at $t' = 0$ from test 11. In all the velocity vector maps shown in this paper, only every other vector in the vertical direction is plotted to avoid cluttering. The solitary wave propagates from right to left, and fluid velocities are positive in the onshore and upward directions. Note the opposite (seaward) direction for x^+ in the abscissa in Fig. 10a. The dimensionless local coordinate is used to locate coherent structures in the measurement area. The measured velocity field contains 57 vector columns in the cross-shore direction. These were spatially averaged over every five neighboring columns (columns 2 to 6, 7 to 11, …., 52 to 56, omitting columns 1 and 56) to produce 11 average velocity profiles for determining the local bed shear stress (see section 2.3). The locations of the 11 average velocity profiles are shown as dashed lines in Fig. 10a.

The velocity field measurements contain some spurious vectors. They were produced by entrained air bubbles in the FOV of the PIV camera. The flume was filled with fresh water a few days before the experiment and left to equalize to room temperature. As the water temperature increased, tiny air bubbles began to form on the Plexiglass bottom and side walls. They could not be completely cleaned, and some were dislodged by the flow during the experiment (see Fig. 5). This usually occurred around the wave crest phase ($t' = 0$ and 1) when the water particle velocities were high. Spurious vectors were removed manually where they could not be filtered out by the vector validation scheme. Because most of the entrained air bubbles were carried in the free stream, their effect on the velocity measurements near the bed was small.

The ensemble-averaged velocity has been subtracted from Fig. 10a to reveal the underlying turbulent coherent structures. Two large counterclockwise vortices can be seen around $x^+ = 500$ and 800, with the remnant of a third vortex around $x^+ = 200$. The vortices are highlighted in Fig. 10a with their direction of rotation. These vortices are like the periodic hairpin vortices captured by the raw image in Fig. 5. The free-stream velocity is at its maximum in Fig. 10a. The ensemble-averaged velocity (mean flow) is directed onshore in the entire measurement area. Therefore, the back flow along the bed ($y^+ \leq 50$) is a low-speed streak. These are elongated zones of low velocity fluid aligned roughly parallel to the flow direction. A streak filament may be 1000 wall units in length and separated from adjacent streaks by 100 wall units. They reside mainly in the viscous sublayer and buffer layer and are not observed above $y^+ >$ 40-50 (Panton, 2001). Low-speed streaks are created by streamwise vortices with counter-rotating vorticity in the wall region. Each vortex collects low velocity fluid from very near the wall into a low-speed zone on one side of the vortex while simultaneously bringing high velocity fluid from above to the wall on the other side of the vortex (see Fig. 12 in Smith, 1996). This process creates the low-speed streaks seen in the many flow visualization studies of turbulent flow in wall boundary layers (e.g., Kline et al., 1967; Acarlar and Smith, 1987).

As the low-speed streak moves downstream it also rises from the wall, thus transporting low-momentum fluid near the wall to the upper layer. This process creates a shear layer with inflectional velocity profile on the top and sides of the low-speed streak. The shear or vorticity layer is unstable and rolls up to form a three-dimensional vortex with longitudinal and transverse vortex structure (see Fig. 9). Mutual induction among different parts of the vortex and stretching and bending by the steep velocity gradient near the wall then deform the vortex into various forms which may include horseshoe and Ω-shaped structures. At the same time, the head and forward portion of the vortex loop move away from the wall due to self-induced movement. Several vortices may be formed depending on the extent of the low-speed streak and the initial external disturbance (Smith, 1984). The three vortices in Fig. 10a are spaced at regular intervals, which suggests that they were generated in a periodic fashion. Low velocity fluid moving away from the bed can be seen at the two vortices around $x^+ = 500$ and 800. The vortex around $x^+ = 200$ had moved away from the bed and reached the edge of the boundary layer at $y^+ \approx 300\nu/u^*$. The three vortices are aligned at an angle of approximately 17° to the bed. A similar series of vortices were observed at $t' = 1$ (not shown), but they were more disorganized, which indicates that the vortices were disintegrating into chaotic, random turbulence. Although our planar PIV measurements cannot reveal the 3D structure of these vortices, the flow pattern observed is reminiscent of the periodic hairpin vortices observed in the experiment of Acarlar and Smith (1987) (see Figs. 5 and 6 in their paper) discussed earlier.

Fig. 10b presents the profiles of the measured velocity u and ensemble-averaged velocity $\widetilde{u}$ at the 11 transects shown in Fig. 10a. Inflection points in the velocity profiles can be seen near the vortex centers at $y^+ \approx 250$, transect 5 and at $y^+ \approx 150$, transect 9. Due to the counterclockwise fluid motion, the instantaneous velocity is higher and lower than the mean velocity, respectively, above and below the vortex center. The three vortices are in different stages of development. The vortex around $x^+ = 200$ had mostly dissipated and only remnants of it can be discerned in Fig. 10a. The breakup of this vortex marks the end of the bursting process, and it can be seen in Fig. 10b that the velocity profiles away from the bed onshore of transect 5 have returned to a

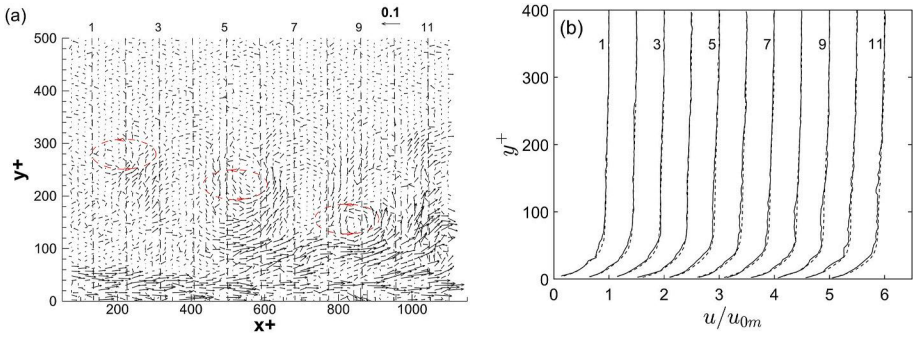

Fig. 10. (a) Turbulent velocity field (u', v') from test 11, $t' = 0$. Only every other velocity vector in the vertical direction is plotted. The solitary wave propagates from right to left. The reference vector is in m/s; and (b) Profiles of nondimensionalized instantaneous velocity (solid line) and ensemble-averaged velocity (dashed line) in the cross-shore direction. Each velocity profile represents the average of 5 vector columns around a vertical transect labeled from 1 to 11 in Fig. 10(a), and u_{0m} is the maximum free-stream velocity at each transect. Each successive velocity profile is offset by a value of 0.5 in u/u_{0m}.

shape like that of the mean velocity profile. The general characteristics of the measured velocity profiles seen in the solitary wave boundary layer are like those observed in the wall boundary layer of steady flows (e.g., Kim et al., 1971).

Fig. 11a presents the turbulent velocity field (u', v') at $t' = 0$ from test 23. This figure shows what appears to be two vortices generated by separate bursting events. The second (offshore) vortex had moved away from the bed and was probably generated before the first (onshore) vortex. The two vortices are separated by a longitudinal distance Δx^+ of about 800 wall units. An inrush of high velocity fluid towards the bed can be seen between $x^+ = 400$ and 600 behind and above the first vortex. Based on flow visualization of turbulent boundary layer flow in a water channel, Offen and Kline (1974, 1975) proposed that sweep motion originating from an earlier burst could trigger new bursting downstream. Their model involves the passage of a previous burst over a low-speed streak. The older burst imposes an adverse pressure gradient on the wall streak and causes it to lift away from the bed. The temporal resolution of our PIV measurements was not high enough to follow the evolution of the vortices, but they suggested that some interactions could have occurred between the two vortices.

Fig. 11b presents the measured velocity profiles at transects 1 to 11 in Fig. 11a. Each vortex has developed a characteristic inflectional velocity profile. An inflection point can be seen in the velocity profile of the offshore vortex around $y^+ = 210$ at transect 9. The measured velocity profile has returned to a shape like that of the mean velocity profile at transect 7, thus marking the end of this event. A new inflectional profile with an inflection point around $y^+ = 100$ can be seen at transect 4 where low velocity fluid is rising from the bed (see Fig. 11a). A velocity excess has also developed away from the bed at transects 3, 4 and 5 due to the inrush of high-speed fluid behind the first vortex.

In addition to counter-clockwise vortices, counter-rotating vortices were also observed. An example from $t' = 0$, test 12 is shown in Fig. 12a. Two counter-rotating vortices, one rotating counter-clockwise and the other clockwise, can be seen over a region of high-speed fluid next to the bed. The counter-rotating vortices were probably a cross section through the two legs of a horseshoe vortex inclined to the bed. As the horseshoe vortex moved away from the bed, it underwent stretching and turning by the background flow. The strong reversed flow between the vortices could be the outward flow induced by the two counter-rotating legs. Fig. 12b shows the measured velocity profiles at transects 1 to 11 in Fig. 12a. The reversed flow between the two counter-rotating vortices creates a large velocity deficit above the inflection points at transects 4, 5, 6 and 7. At the same time, the high-speed streak along the bed causes the instantaneous velocity and velocity gradient to increase below $y^+ < 50$.

Fig. 13a shows the turbulent velocity field (u', v') associated with a strong sweep event from $t' = 0$, test 19. There are some similarities between the measured velocity field in this event and the one shown in Fig. 12a. Both involve a counter-clockwise vortex or a pair of counter-rotating vortices over a high-speed streak or an inrush of high velocity fluid towards the bed. The latter could be the return of a portion of the fluid from the breakup of another bursting event further offshore (Offen and Kline, 1975), or the entrainment of high-momentum fluid from the upper layer by the self-induced flow around a horseshoe vortex (Smith, 1984). Our 2D velocity measurements were unable to distinguish between these events. In both cases, the inrush of high-momentum fluid caused the instantaneous velocity to be higher than the mean velocity near the bed. Fig. 13b presents the velocity profiles at the 11 transects in Fig. 13a. As seen, a region of velocity excess extends from the bed to $y^+ \approx 200$ over much of the measurement area. Such events would produce a high velocity gradient adjacent to the bed and increase the bed shear stress; this will be discussed in section 3.3.

Counter-clockwise vortices or counter-rotating vortices like those shown in Fig. 10a, 11a and 12a and 13a were observed in most of the tests. A back flow or forward flow was often present along the bed, which may be associated with a low-speed streak or an influx of high-momentum fluid from the outer region. Our PIV measurements are consistent with the DNS results of Costamagna et al. (2003) and Scandura et al. (2016), who found that the coherent structures in the near-wall region of oscillatory boundary layers consist of alternating streaks of low- and high-speed fluid roughly aligned with the streamwise flow direction. Their numerical simulations showed that low-speed streaks are lifted from the bed near the end of the acceleration phases or in the early part of the decelerating phases. The transport of low-momentum fluid from the wall region to the outer region creates an inflection in the instantaneous velocity profile. The shear layer thus created is unstable and rolls up to form a transverse vortex, which is then stretched by the mean flow gradient to produce a horseshoe or hairpin vortex with two counter-rotating legs. In the final stage of the bursting process, the hairpin vortex moves away from the bed and breaks down into random, chaotic turbulence. The sampling rate of our PIV measurements was not high enough to capture a complete sequence of streak lifting, vortex generation and breakup under the solitary wave. However, discrete images from repeated experiment runs lend support to a turbulence generation process like that in the wall boundary layer of steady flows described by Kim et al. (1971) and others. As in oscillatory flows, these events occurred under the solitary wave at about the same phase in different experiment runs instead of randomly in space and time as in the case of steady flows.

Similar flow structures were observed during the second period of turbulence production from $t' = 4$ to 8. An example from $t' = 8$, test 18, is presented in Fig. 14. Note that the flow area shown is about the same as at $t' = 0$, but the wall region ($y^+ < 30$) is much thicker at $t' = 8$ due to the small value of u^* around near-bed flow reversal. The structure of the counter-rotating vortices resembles the model of ejection and sweep described in Nakagawa and Nezu (1981) and Smith (1984). These authors proposed that the ejection and sweep events prevalent in turbulence measurements of wall boundary layer flows are the result of outward and wall-ward flows induced by horseshoe/hairpin vortices. Specifically, the up flow between the two counter-rotating legs entrains

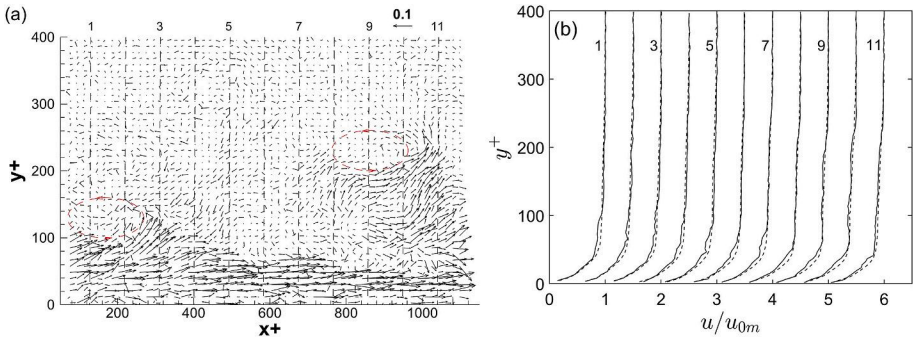

Fig. 11. Same as in Fig. 10, but for test 23.

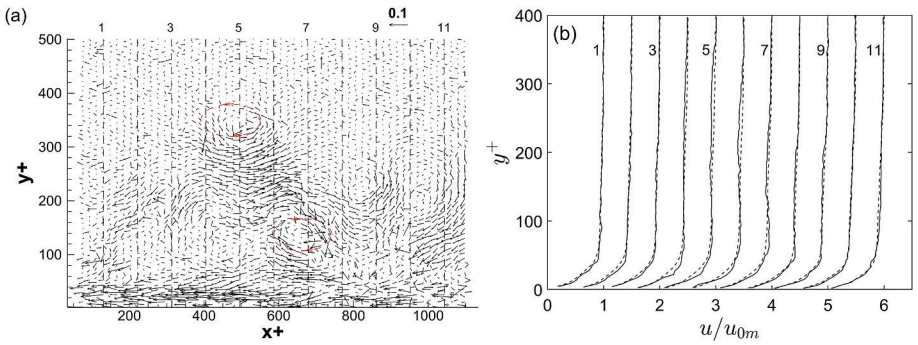

Fig. 12. Same as in Fig. 10, but for test 12.

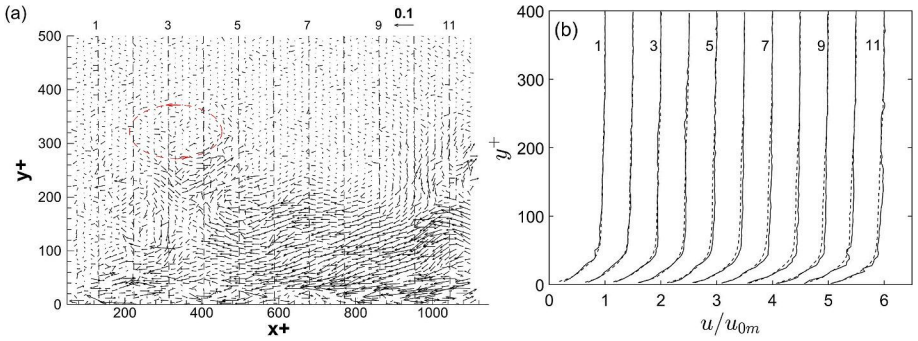

Fig. 13. Same as in Fig. 10, but for test 19.

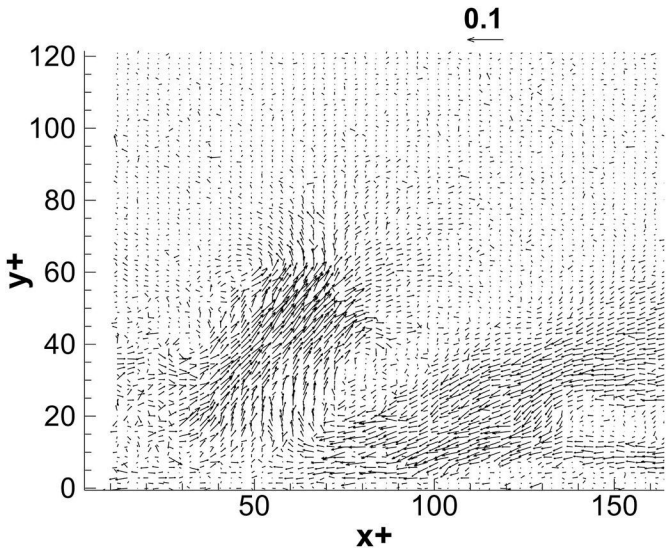

Fig. 14. Turbulent velocity field (u', v') from test 18, $t' = 8$. Only every other velocity vector in the vertical direction is plotted. The solitary wave propagates from right to left. The reference vector is in m/s.

low-momentum fluid from the low-speed streak and pumps it upward (ejection), while the down flow around the outside of the vortex loop brings high-speed fluid from the outer layer towards the wall (sweep). This process is depicted by the wide arrows in Fig. 9. Hence, ejections and sweeps are complementary motions in the bursting process. Since the hairpin vortex is inclined to the bed, an ejection and a sweep would appear as a Q_2 and a Q_4 event, respectively, in a quadrant analysis of the fluctuating turbulence velocities u' and v'. This relationship between u' and v' can be readily discerned in the PIV measurements shown in Fig. 14, where the ensemble-averaged velocities have been subtracted to reveal the turbulent velocity fluctuations. Smith (1984) further proposed that as the hairpin vortices break up and dissipate, remnants of their stretched legs would coalesce into longer streamwise vortices, which in turn form new low-speed streaks. In this manner, turbulence becomes self-sustaining when new wall streaks are generated by the hairpin vortices which in turn generate new hairpins.

After near-bed flow reversal, a region of negative (seaward) velocities developed adjacent to the bed. The mean velocity profile develops an inflection point which migrates steadily upwards as more of the boundary layer came into flow reversal. Such a velocity profile, with a vorticity maximum at the inflection point, is unstable and will trigger the Kelvin-Helmholtz instability when the Reynolds number is sufficiently large (Panton, 1984). An example from test 7, $t' = 11$ is shown in Fig. 15a, where the measured velocity field (u, v) is presented without ensemble average subtraction. The abscissa and ordinate are normalized by the thickness of the boundary layer δ, which is equal to 15.4 mm at this phase. The thickness of the shear layer is around 0.1δ. The velocity magnitude inside the shear layer is small, but the velocity gradient is large. Three counterclockwise vortices can be seen with their centers located inside the vorticity layer. The general locations and direction of rotation of the vortices are indicated in the figure. Fig. 15b shows the measured velocity field (u, v) from the same test at $t' = 12$. The free stream is now at flow reversal. The shear layer formed is marked by wavelike undulations separating the nearly zero velocities in the free stream and the negative velocities inside the boundary layer. The KH vortices are not evident with the mean flow superimposed, but they become visible after the mean flow is subtracted. The approximate location and extent of the vortices are marked in the figure. The diameter of the vortices is around 0.4δ and their horizontal and vertical velocities are highly correlated, which would produce efficient mixing of fluid momentum. From $t' = 8$ to $t' = 12$, the thickness of the boundary layer increases by about 50%, from 10.7 mm to 16 mm (see Fig. 2).

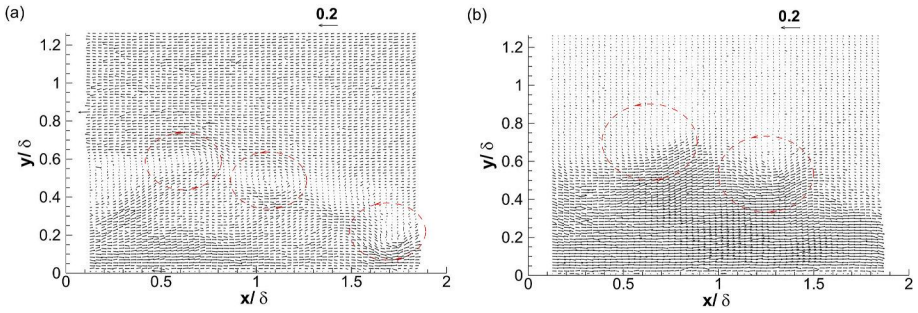

Fig. 15. (a) Measured velocity field (u, v) without ensemble average subtraction from test 7, $t' = 11$ and (b) $t' = 12$. Only every other velocity vector in the vertical direction is plotted. The solitary wave propagates from right to left. The reference vector is in m/s.

3.3. Instantaneous bed shear stresses and quadrant analysis

It is evident from the measured velocity profiles that an ejection event would reduce the velocity gradient near the bed, while a sweep would have the opposite effect. The effect on the instantaneous bed shear stress at $t' = 0$ is shown in Fig. 16 for tests 12 and 23. The bed shear stress τ_b at each of the 11 vertical transects in the measured velocity field is normalized by the FOV- and ensemble-averaged bed shear stress $< \widetilde{\tau_b} >$. In test 12, the prevalence of sweep events adjacent to the bed (see Fig. 12a) produces instantaneous bed shear stress values mostly higher than the average bed shear stress (top plot). The ratio of the maximum local bed shear stress to the average bed shear stress is 1.4. In test 23, the prevalence of ejection events adjacent to the bed (see Fig. 11a) produces instantaneous bed shear stress values mostly below the average bed shear stress, with a minimum $\tau_b / < \widetilde{\tau_b} >$ ratio of 0.65.

It is also evident that ejections and sweeps are prevalent in the PIV measurements. To identify turbulent events that produce large bed shear stress fluctuations, we divide the measured bed shear stress values into four quadrants (Q_1 to Q_4) based on the signs of the turbulent velocity components u' and v' and compute their probability distributions. In the (x, y) coordinate system, $u' > 0$ and $v' > 0$ correspond to quadrant Q_1 or outward interaction; $u' < 0$ and $v' > 0$ correspond to quadrant Q_2 or ejection; $u' < 0$ and $v' < 0$ correspond to quadrant Q_3 or inward interaction; and $u' > 0$ and $v' < 0$ correspond to quadrant Q_4 or sweep (Nezu and Nakagawa, 1993). Fig. 17 shows the results of quadrant analysis at selected locations in the measured velocity fields at $t' = 0$ from tests 11, 12, 19 and 23. In test 11 (see Fig. 10a), the large counterclockwise vortex around transect 6 produces large turbulent velocity fluctuations that fall primarily in quadrant Q_2 and are classified as ejection events. Similarly, at transect 6, test 12 (see Fig. 12a), ejections are associated with the backward ($u' < 0$) and upward ($v' > 0$) flow induced between the two counter-rotating vortices. Hence, the measured turbulent velocity fluctuations lie primarily in quadrant Q_2, while the inrush of high-speed fluid ($u' > 0$ and $v' < 0$) adjacent to the bed represents sweeps which show up as Q_4 events in the quadrant plot. The Q_1 events ($u' > 0$ and $v' > 0$) are associated with the clockwise vortex, but there are relatively few of them compared to the Q_2 and Q_4 events. Two other examples from test 19, transect 6 (see Fig. 13a) and test 23, transect 3 (see Fig. 11a) involve an inrush of high velocity fluid toward the bed (test 19) and the lift-up of low-speed streaks (test 23), are expressed as Q_4 (sweep) and Q_2 (ejection) events, respectively, in the quadrant plots.

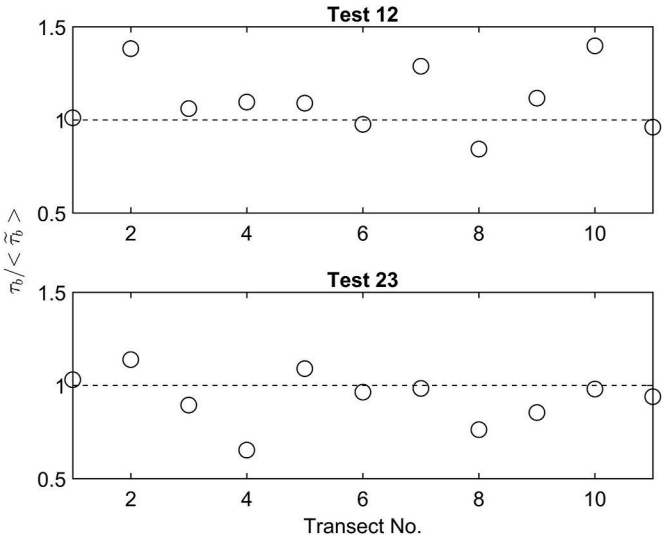

Fig. 16. Ratio of local bed shear stress to FOV- and ensembled-averaged bed shear stress at transects 1 to 11, $t' = 0$, tests 12 and 23.

To investigate the probability of large bed shear stresses induced by coherent structures, the measured bed shear stresses at transects 1 to 11 from all 20 experiment runs (total 220 instantaneous bed shear stress values) are sorted into four quadrants (Q_1 to Q_4) based on the mean values (denoted below by an overbar) of u' and $u'v'$ computed in the viscous sublayer and buffer layer ($0 < y^+ < 30$), where quadrant Q_1 is determined by $\overline{u'} > 0$, $\overline{u'v'} > 0$; quadrant Q_2 by $\overline{u'} < 0$, $\overline{u'v'} < 0$; quadrant Q_3 by $\overline{u'} < 0$, $\overline{u'v'} > 0$; and quadrant Q_4 by $\overline{u'} > 0$, $\overline{u'v'} < 0$. Note that u' and v' are positive in the onshore and upward direction, respectively. Fig. 18 shows the probability distributions of instantaneous bed shear stress in the four quadrants (from top to bottom) at $t' = 0$, 1 and 2 (from left to right). Probability is computed as the number of events that falls within a specified bed shear stress interval divided by the total number of events in the same quadrant and expressed as a proportion between 0 and 1. In the abscissa, x denotes the instantaneous bed shear stress, and μ and σ are the mean and standard deviation of bed shear stress values from all four quadrants. The left plots ($t' = 0$) show that at the onset of turbulence, there are more Q_1 and Q_2 events (67 each) than Q_3 and Q_4 events (40 and 46, respectively). This is related to the lift-up of low-speed streak and roll-up of the shear layer seen in Fig. 5. The left plots also show that the probability distributions of instantaneous bed shear stress corresponding to Q_1 and Q_4 events are positively skewed with extremum values ranging from 2 to 3 times the standard deviation above the mean, while Q_2 and Q_3 events produce instantaneous bed shear stress values mostly below the mean. The results for $t' = 1$ and 2 are presented in the center and right plots. The probability distributions of instantaneous bed shear stress in the different quadrants show similar trends as those at $t' = 0$ in terms of the effect of u' and v' on the bed shear stress. However, the number of Q_4 events has increased significantly and is close to the number of Q_2 events, which means that sweep events have become more common in the later stage of the bursting process and are complementary to ejection events. Furthermore, Q_4 events are responsible for producing large instantaneous bed shear stress values as high as four to five times the standard deviation above the mean. In comparison, there are much fewer Q_1 and Q_3 events therefore they are of lesser

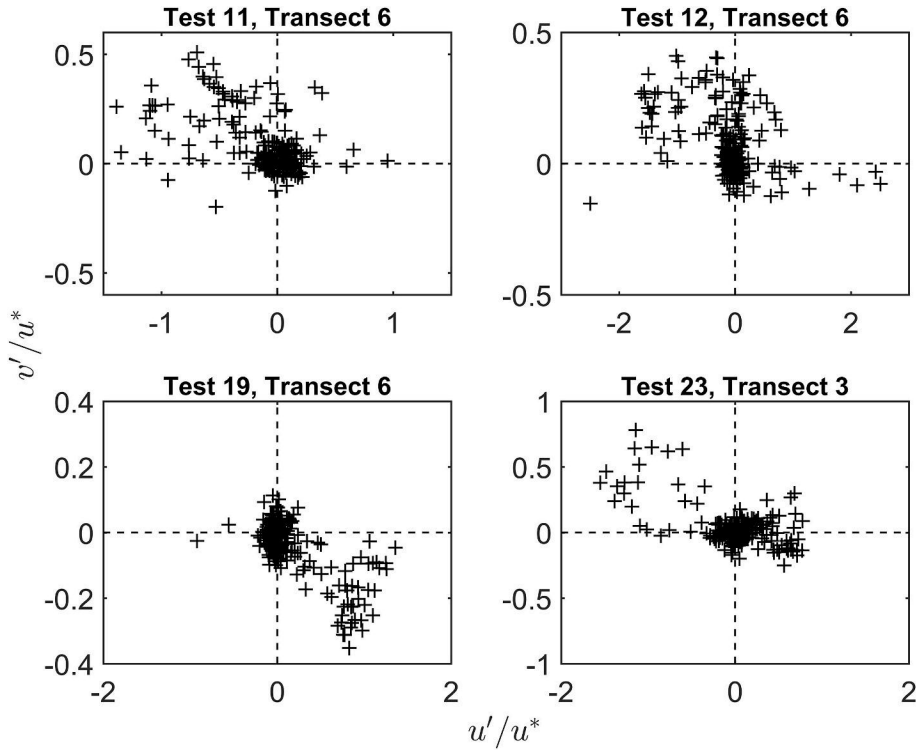

Fig. 17. Quadrant plots of normalized turbulent velocity fluctuations u' and v' from selected locations at $t' = 0$, tests 11, 12, 19 and 23.

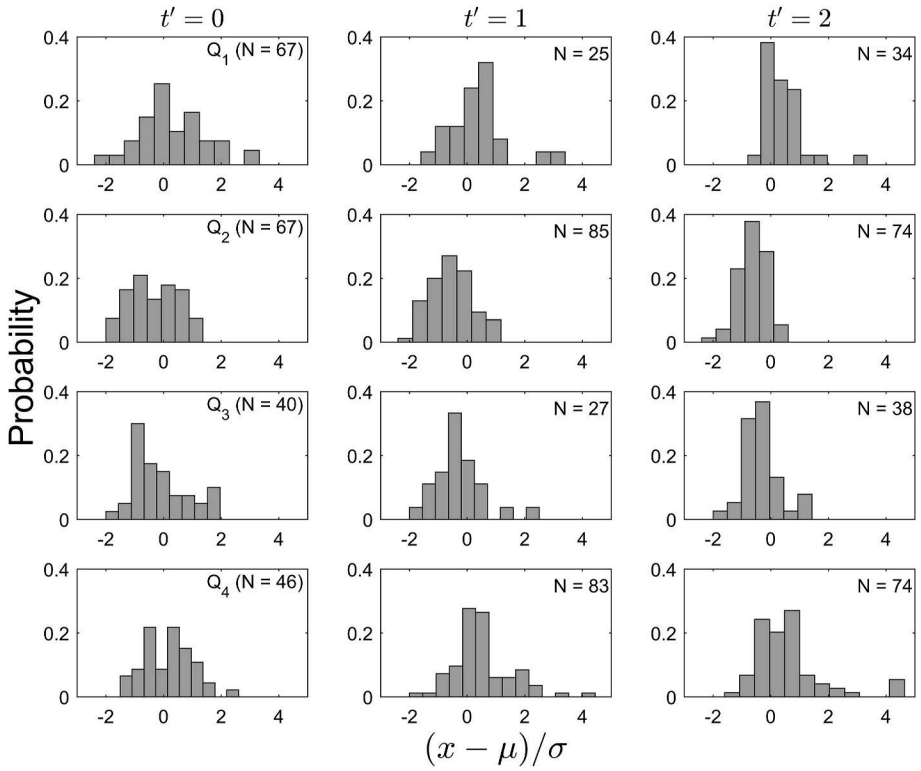

Fig. 18. Probability distributions of local bed shear stress in quadrants Q_1 to Q_4 (from top to bottom) at $t' = 0, 1$ and 2 (from left to right). The values of μ and σ (in N/m^2) at the different times are: 1.66 and 0.32 ($t' = 0$), 1.3 and 0.39 ($t' = 1$), and 0.81 and 0.24 ($t' = 2$).

importance in producing extremum values of instantaneous bed shear stress.

3.4. The law of the wall

Eq. (4) is often used in numerical simulations of wall-bounded flows to relate the wall shear stress to the velocity in the outer layer, thereby

avoiding the need to resolve the high velocity gradient across the viscous sublayer and buffer layer. In RANS models, the mean flow is computed, and Eq. (4) is applied directly to the ensemble-averaged velocities. In models that employ Large-Eddy Simulation (LES), spatial filtering as opposed to ensemble averaging is applied to the momentum equations (Pope, 2000). If the fluid acceleration and pressure gradient terms in the filtered momentum equation in the streamwise direction are assumed to balance exactly, a logarithmic law of the wall like Eq. (4) for the filtered fluid velocity can be derived by integrating the resulting ordinary differential equation (ODE) with the eddy viscosity given by a mixing length model (see Larsson et al., 2015). Alternatively, Eq. (5) may be used to model the velocity profile in the viscous sublayer through the buffer layer and into the logarithmic layer. As an example, Zhou et al. (2014, 2017) used Eq. (5) with an LES model to compute the bed shear stress induced by breaking-wave-generated vortices in a laboratory surf zone, even though the general validity of the law of the wall in non-equilibrium turbulence has not been proven. In their LES models, it was also assumed that Eq. (5) could be applied locally and instantaneously to a three-dimensional (3D) velocity field.

In LES, the large-scale motions (large eddies) of turbulent flow are computed directly but the small-scale motions (small eddies) are modeled. Since velocity vectors are computed at the cell centroids in LES simulations, it will require a minimum of 4 grid cells to resolve an eddy. For the vortices observed in this study (e.g., Fig. 10a), this requirement would result in a streamwise grid size $\Delta x^+ \approx 100$. At this grid resolution or finer, the local equilibrium assumption is likely incorrect, and Eqs. (4) and (5) may not be valid. As discussed in Piomelli and Balaras (2002), the near-wall grid must be very coarse to contain many eddies for their average effect to be represented by a logarithmic law of the wall.

A filter function commonly employed in LES models is the box filter, which is simply the spatial moving average of the velocity field. The latter is akin to the local averaging of velocity profiles performed in this study. The local averaging was performed over 5 neighboring vector columns in the measured velocity fields, which resulted in a spatial resolution $\Delta x^+ \approx 70$. At this resolution, the local velocity profile and bed shear stress induced by the large vortices are resolved. In this section, we examine how well these local average velocity profiles follow the law of the wall. With $A = 2.5$ and u^* determined by fitting a straight line to the measured velocity data in the viscous sublayer, the value of B and the extent of the logarithmic region (if existed) are found by fitting Eq. (5) to the average velocity profile at each of the 11 transects in the measured velocity fields. The data analysis is performed at $t' = 2$ when the boundary layer is fully turbulent and there is good agreement between the ensemble-averaged velocity profiles and Eq. (5) (see Fig. 8). A total of 220 velocity profiles (11 profiles/run × 20 experiment runs) were inspected manually and grouped into six separate categories (cases A through F) as described below.

Fig. 19 shows an example of each case. In cases A and B, a logarithmic region exists but the value of B may have a value different from 5.0. Cases A and B also differ in the measured velocity distribution in the buffer layer, which generally follows the Spalding wall function given by Eq. (5) in case A but not in case B. In case C, a logarithmic region does not exist but the velocity profile in the buffer layer still follows Eq. (5). In case D, the velocity profile deviates from Eq. (5) outside the viscous sublayer and the profile cannot be classified as one of the other types. In cases E and F, the measured velocity profiles exhibit large oscillations, which occur outside the buffer layer in case E but also inside the buffer layer in case F. Based on the above classification, there are 77 (35%), 27 (12%), 34 (15%), 2 (1%), 37 (17%) and 43 (20%) profiles in cases A through F, respectively. Inevitably, classifying the borderline cases can be somewhat subjective, and this should be kept in mind when interpreting the statistics. It is also noted that the value of B in Eq. (4) is very sensitive to the value of u^*. Therefore, the difference between cases A and B may in some cases be simply due to the uncertainty in determining u^*.

In 35% of the cases (case A), the instantaneous velocity distribution follows Eq. (5) well. This is the assumption commonly used in LES models that employ the law of the wall. If the first computational point is placed in the logarithmic layer, Eq. (4) may be used to calculate the bed shear stress to provide the wall boundary condition for the momentum equations (see Piomelli and Balaras, 2002). The value of B is not equal to 5.0 in case B, but a logarithmic region still exists so that the bed shear stress may be calculated using Eq. (4) but it will require a minimum of two velocity points in the logarithmic layer to determine the slope of the best-fit line and then the bed shear stress. If the first near-wall point is placed in the buffer layer, the Spalding wall function (Eq. (5)) may be used to calculate the friction velocity in cases A, C and E, which

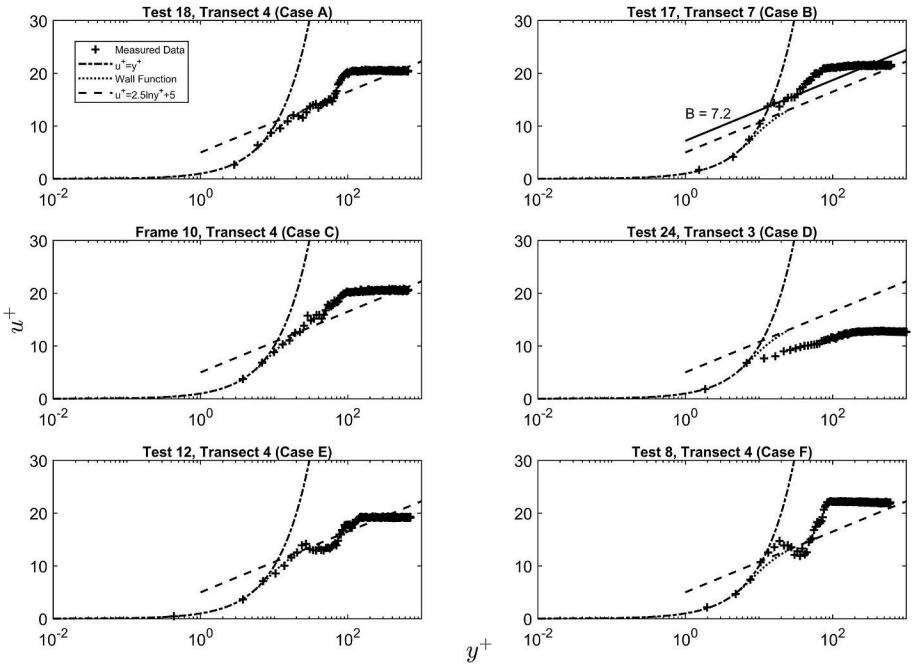

Fig. 19. Examples of the measured velocity profile in cases A through F in semi log plot, $t' = 2$. Each profile is the average of 5 neighboring vector columns.

comprise 67% of the velocity profiles at $t' = 2$.

The velocity profiles in cases E and F are characterized by large oscillations in the buffer layer and/or outer layer. PIV measurements show that the oscillations are associated with large vortices and/or influx of high-momentum fluid towards the bed. Two examples are presented in Figs. 20 and 21, in which the velocity profile at each transect is identified with one of the six cases described above. In Figs. 20 and 21, the edge of the boundary layer is located at $y^+ \approx 200$. Note that cases E and F are found around the large transverse vortices.

The breakup of the large vortices was often observed with an influx of high-speed fluid towards the bed. This can be seen in both Figs. 20 and 21 (see the region between transects 1 and 3). In Fig. 21, the high-speed fluid adjacent to the bed behind the vortex around $x^+ = 400$ could have originated from another bursting event offshore, which then interacted with the slow-moving fluid in the wall region to initiate the lift-up of a low-speed streak and formation of the large counterclockwise vortex seen in the figure. In turn, the breakup of this vortex created a strong wall-ward flow towards the bed, which could induce the lift-up of new wall streaks farther onshore. The observed phenomenon is consistent with the bursting process described by Offen and Kline (1974, 1975) discussed earlier in section 3.2.

Fig. 22 shows the probability distributions of bed shear stress grouped by the six categories described above. Probability distribution is expressed as a proportion between 0 and 1, x denotes the instantaneous bed shear stress, and μ and σ are the mean and standard deviation of bed shear stress from all 220 velocity profiles. Only two velocity profiles are found in case D. They are associated with measured bed shear stresses much greater than the mean. For further analysis, case D has been combined with case F. Each bed shear stress value is also assigned one of the four quadrants (Q_1 to Q_4) based on the mean values of u' and $u'v'$ in the viscous sublayer and buffer layer (see section 3.3). These results are used to examine the relationship between the shape of the instantaneous velocity profiles and bursting events in the wall layer.

Case A comprises 77 profiles, of which 13, 29, 15 and 20 are Q_1, Q_2, Q_3 and Q_4 events, respectively. There are about an equal number of Q_1 and Q_3 events, and they are substantially less than the number of Q_2 and Q_4 events. The probability distribution of the instantaneous bed shear stress is negatively skewed due to the large number of ejection events. These characteristics are consistent with a turbulent boundary layer in which the velocity profile conforms to the law of the wall. Similar results may be found in the probability density distribution of $u'v'$ in oscillatory boundary layer flow in Hino et al. (1983).

Case B comprises 27 profiles, of which 3, 10, 1, and 13 are Q_1 to Q_4 events. The probability distribution of instantaneous bed shear stress is more uniformly distributed compared to Case A. Case C comprises 34 profiles, of which 3, 13, 13 and 5 are Q_1 to Q_4 events. The large number of Q_2 and Q_3 events produce a probability distribution with instantaneous bed shear stress values mostly below the mean. Case E comprises 37 profiles, of which 8, 11, 4 and 14 are Q_1 to Q_4 events. The probability distribution of bed shear stress is weakly positively skewed. Cases D and F comprise 45 profiles, of which 7, 9, 7 and 22 are Q_1 to Q_4 events. The prevalence of sweep events produces a probability distribution that is

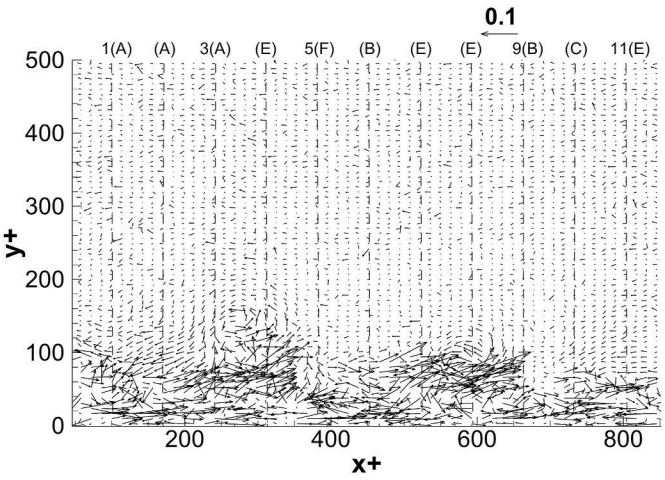

Fig. 20. Turbulent velocity field (u', v') from test 12, $t' = 2$. Only every other velocity vector in the vertical direction is plotted. The solitary wave propagates from right to left. The reference vector is in m/s. The locations where the different cases (A to F) are found are indicated in the figure.

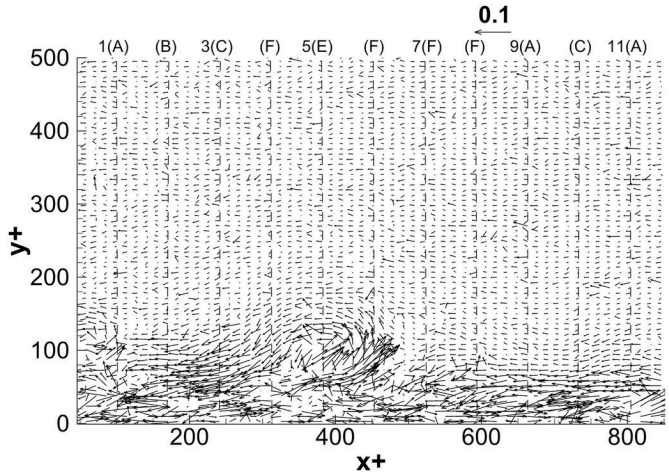

Fig. 21. Same as in Fig. 20, but for test 8.

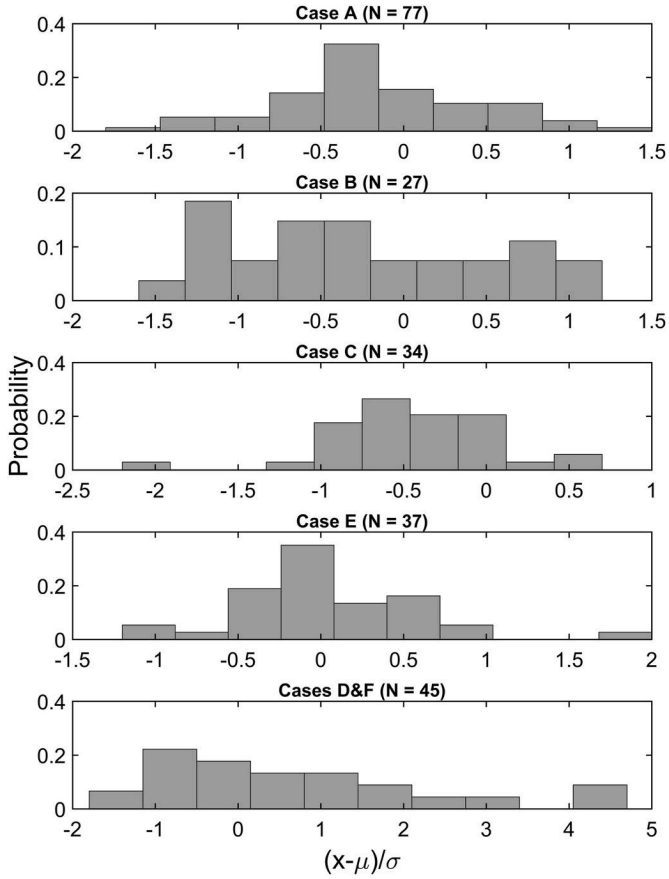

Fig. 22. Probability distributions of instantaneous bed shear stress in cases A through F at $t' = 2$. The values of μ and σ (in N/m^2) are 0.81 and 0.24, respectively.

strongly positively skewed with instantaneous bed shear stress values mostly above the mean. This plot shows that a high proportion of the instantaneous velocity profiles that do not conform to the law of the wall (cases D and F) are associated with sweep events in the viscous sublayer and buffer layer. This phenomenon may be related to the influx of high-momentum fluid towards the bed discussed earlier.

Fig. 23 shows the histograms for B and extent of the logarithmic region δy^+ in wall units for cases A and B together. The largest subgroup of B values (39 profiles) lie in the range of 4.5–5.5, with a decreasing number of velocity profiles towards larger values of B. This is consistent with the distribution of the ensemble-averaged velocities found in previous studies (e.g., Hino et al., 1983; Mier et al., 2021). Specifically, the value of B changes for different phases of the period in oscillatory flows. It decreases at the end of the acceleration phases and reaches a constant value between 5.0 and 5.5 in the later part of the deceleration phases. We have seen in Fig. 8 that the ensemble-averaged velocities do not develop the full "law-of-the-wall" profile until $t' = 2$. Therefore, the positively skewed distribution of B in the instantaneous velocity profiles seen in Fig. 23 is consistent with this observation. The bottom plot in Fig. 23 shows that the logarithmic region in the instantaneous velocity profile, if exists, is very narrow, with δy^+ being less than 30 in 58 out of 104 profiles. This result also agrees with the distribution of ensemble-averaged velocities in oscillatory boundary layer flows in the transitional turbulent regime (e.g., Jensen et al., 1989; Scandura et al., 2016).

The measured instantaneous velocities conform more to a law-of-the-wall velocity profile when the size of the averaging window is increased. Fig. 24 compares the result of averaging 5 neighboring vector columns with the result of averaging 20 vector columns around the counter-clockwise vortex at $x^+ \approx 270$ in Fig. 20. The larger averaging window has a width of $\Delta x^+ \approx 270$, which is comparable to the diameter of the vortex. As seen, the large oscillations are smoothed out and a small logarithmic region now exists just outside the buffer layer. Spatial averaging was performed on 50 vortices drawn from 20 experiment runs. The number of vector columns averaged varied from 15 to 30 ($\Delta x^+ \approx 200$ to 400) depending on the size of the individual vortices. It was found that case F comprised only 14% of the velocity profiles when the larger averaging windows were used. In addition, the average velocities were much closer to a law-of-the-wall velocity profile. When the measured velocities are averaged over the entire FOV (55 vector columns, excluding columns 1 and 57), the resulting 20 FOV-averaged velocity profiles contain 8, 3, 7, 0, 1 and 1 profiles in cases A through F, respectively. The FOV-averaged velocity profiles from tests 8, 10 12, 17, 18 and 24 are presented in Fig. 25. Compared to the local average velocity profiles in Fig. 19, the FOV-averaged velocity profiles are much closer to Eq. (5). However, the average velocity profiles may not yield the correct local bed shear stresses if the averaging window is too large. Fig. 26 shows the probability distribution of bed shear stress determined from the local average velocity profiles around the 50 vortices. The results are normalized by the bed shear stresses determined from the corresponding FOV-averaged velocity profiles. In over half of the cases, the average bed shear stresses around the vortices deviate from the FOV averages by more than 10%. Therefore, local bed shear stresses could be significantly overestimated or underestimated when using an averaging window much larger than the size of the vortices.

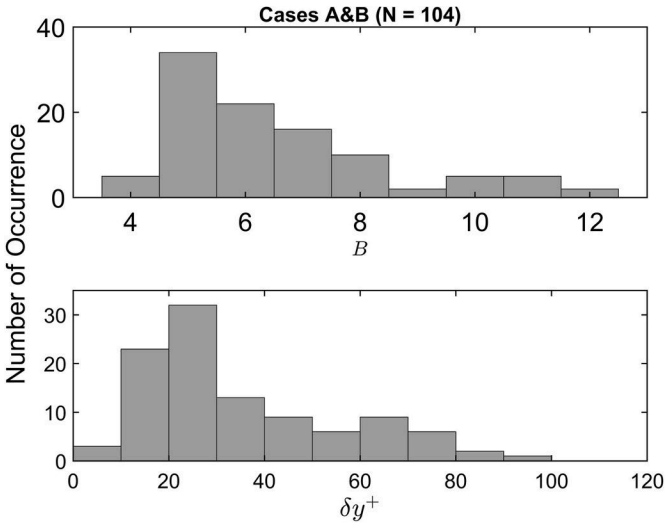

Fig. 23. Histogram plots of log law intercept B and extent of logarithmic region δy^+ for the instantaneous velocity profiles in cases A and B, $t' = 2$.

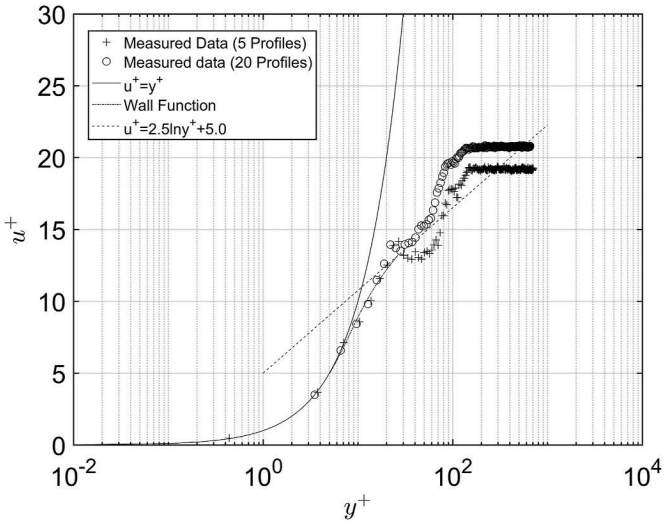

Fig. 24. Effect of averaging window size on the instantaneous velocity profile. The measured velocities are from test 12, $t' = 2$. The profile denoted by "+" is the average of 5 vector columns around the vortex centered at $x^+ \approx 270$, and the profile denoted by "o" is the average of 20 vector columns around the same vortex.

4. Discussion and conclusions

We have examined the coherent structures generated in the bottom boundary layer of a solitary wave near the point of incipient breaking. The velocity field was captured using a planar PIV system. The bed was smooth, and the wave Reynolds number was in the intermittent turbulent regime. Previous studies of coherent structures in oscillatory boundary layers were conducted mostly in water tunnels, where a free surface was absent, and the longitudinal pressure gradient was uniform. Our PIV measurements captured the history of the mean flow and turbulence, including the near-bed flow reversal during flow deceleration and the change in direction in the bed shear stress. It was found that the mean bed shear stress reached its peak at about the same time as the free-stream velocity. The measured maximum bed shear stress was greater than the value obtained using the friction factor diagram in Sumer et al. (2010). The latter was developed for symmetric solitary flow motion in a water tunnel. It was found that a logarithmic layer existed in the ensemble-averaged velocity profiles for only a brief time during flow deceleration, consistent with an unsteady-flow boundary layer in the intermittent turbulent regime. The distributions of root-mean-square turbulence velocities and Reynold stress were investigated and compared with steady and oscillatory boundary layer flows.

The measured velocity fields showed that the basic characteristics of the turbulent coherent structures in a solitary wave boundary layer were like those observed in oscillatory boundary layers at similar wave Reynolds numbers. Turbulence was suppressed during the acceleration phases but grew explosively at the beginning of flow deceleration with

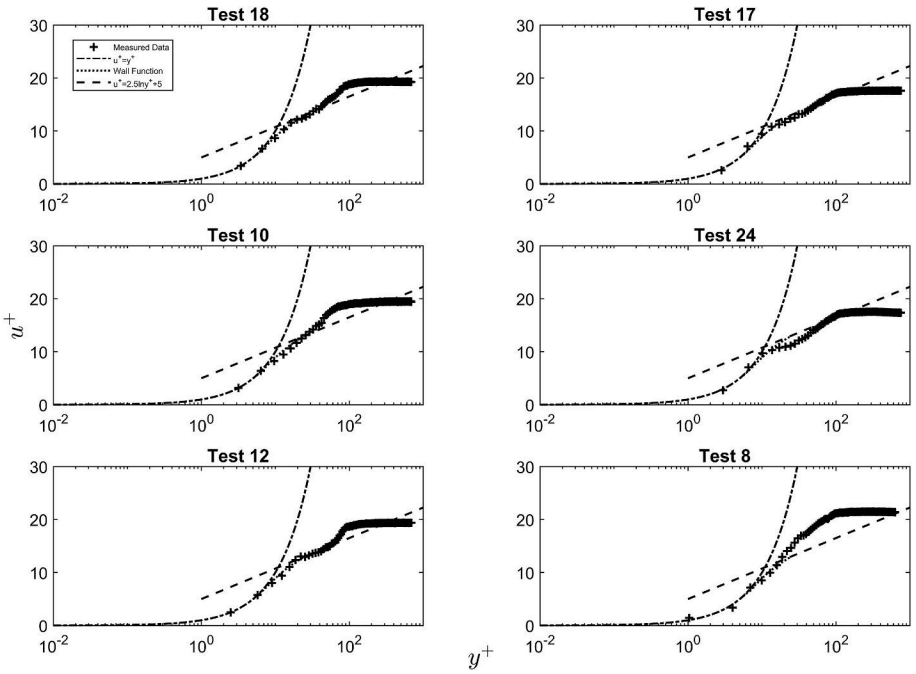

Fig. 25. Same as in Fig. 19, but each velocity profile is the FOV average over 55 vector columns.

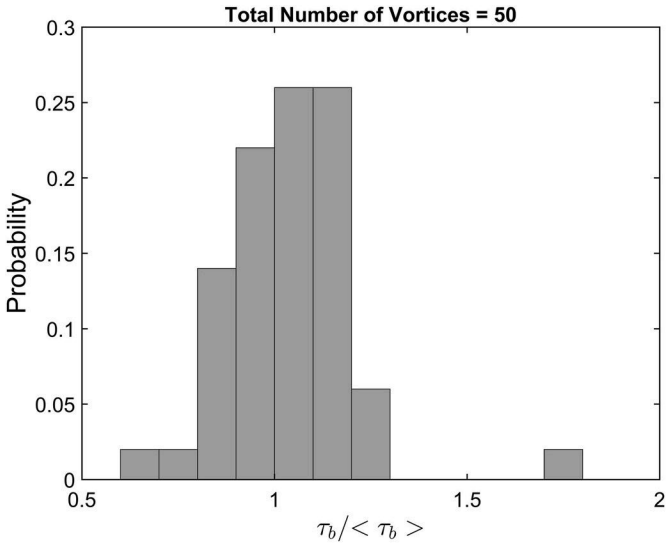

Fig. 26. Probability distribution of local bed shear stress around 50 vortices from 20 experiment runs. The average bed shear stress around each vortex has been normalized using the bed shear stress determined from the FOV-averaged velocity profile in the corresponding experiment.

the lifting of low-speed fluid from the bed and formation of transverse vortices. Large counter-rotating vortices were also observed which might be related to the horseshoe vortices discussed in the literature. Transverse vortices were observed in isolation or in a group of 2–3 aligned after one another as they moved away from the bed. As the vortices decayed, the turbulence intensity decreased, but a second period of turbulence production and vortex generation occurred before near-bed flow reversal. A shear layer then developed between the reversed flow near the bed and the shoreward flow away from the bed. Kelvin-Helmholtz (KH) vortices were generated and advected offshore. The shear layer migrated upward as more of the flow away from the bed reversed direction. The thickness of the boundary layer also increased due to mixing of momentum by the large roll vortices.

The temporal resolution of our PIV measurements was not high enough to follow the generation and evolution of the vortices in time. In addition, the velocity measurements were confined to the longitudinal vertical plane therefore information on the 3D flow field was incomplete. Nevertheless, useful conclusions can be drawn by observing these 2D flow measurements from repeated experiment runs. The mechanisms that generated and maintained turbulent coherent structures in a solitary wave boundary layer appeared to be like those in steady flows. Specifically, streak-lifting produces inflectional velocity profiles that are unstable, and the roll-up of shear layers leads to the formation of hairpin vortices. Ejections and sweeps work together to maintain the bursting process. Sweep events were seen as wall-ward movement of high-momentum fluid generated by the breakup of transverse vortices (e.g., Offen and Kline, 1974, 1975), and as wall-ward induction effects created by counter-rotating vortices (e.g., Nakagawa and Nezu, 1981; Smith, 1984). On the other hand, ejections manifested themselves in the lifting of low-speed streaks and pumping of low-momentum fluid upward by the vortices. Our PIV measurements support the notion that boundary layer turbulence is triggered and maintained by flow instabilities in the wall region then spreads to the outer layer.

The unique contribution of this study, however, is in the simultaneous measurements of the velocity field of turbulent coherent structures and bed shear stress. The latter was obtained by a fitting a straight line to the measured velocity points very close to the bed and employing the Newton's law of viscosity. The simultaneous, whole (2D) flow field measurements of water particle velocity and bed shear stress allow us to examine the effects of coherent structures on the near-bed velocity profile and instantaneous bed shear stress not possible in previous studies that employed single-point measurement techniques such as LDA and hot-film probe or shear plate. The results showed that ejection events in the viscous sublayer and buffer layer generally decreased the velocity gradient close to the bed and reduced the instantaneous bed shear stress, while sweep events had the opposite effect. Quadrant analysis based on the turbulence velocity components u' and v' showed that Q_2 and Q_4 events had about the same number of occurrences when the boundary layer was fully turbulent, which suggests that ejections and sweeps are complementary processes in generating and maintaining turbulence. The probability distribution of bed shear stress for Q_4 events was positively skewed, while that for Q_2 events was negatively skewed.

It was found that Q_4 events were responsible for producing instantaneous bed shear stress fluctuations as large as four to five times the standard deviation above the mean, while Q_2 events produced instantaneous bed shear stress values mostly below the mean. In comparison, there were much fewer Q_1 and Q_3 events therefore they were of lesser importance in producing extremum values of bed shear stress.

The existence of the law of the wall was investigated for the measured velocities without ensemble averaging. The problem is relevant to the implementation of wall functions in LES models, where spatial filtering rather than ensemble averaging is applied to the LES equations. It was found that the value of the logarithmic layer intercept B was very sensitive to the uncertainties in the friction velocity. When the boundary layer was fully turbulent, the measured instantaneous velocities were predicted well by the Spalding wall function to the top of the buffer layer in 67% of the cases. Large oscillations in the measured profiles were found outside the buffer layer in about 17% of the cases and in the buffer layer in another 20% of the cases. In the latter, about half (47%) were associated with Q_4 events, compared to 21% for Q_2 events and 16% each for Q_1 and Q_3 events. Therefore, a high proportion of the instantaneous velocity profiles that did not conform to the law of the wall were associated with sweep events in the viscous sublayer and buffer layer. It was also found that the instantaneous velocities did not conform to a law-of-the-wall velocity profile unless the averaging window was at least several times larger than the size of the vortices. Our results show that the law of the wall only holds instantaneously when the measured velocities are averaged over an area large compared to the coherent structures. This was also suggested by Piomelli and Balaras (2002). Indeed, Mason and Callen (1986) succeeded in applying the logarithmic law instantaneously in LES modeling of turbulent channel flows only by using very large grid sizes ($\Delta x/\delta$ between 0.15 and 0.6).

This study has examined the coherent structures in the bottom boundary layer of a near-breaking solitary wave using 2D PIV. Currently, we are conducting three-dimensional, three-component (3D3C) velocity measurements in the bottom boundary layer of solitary waves using a volumetric three-component velocimetry (V3V) system. The experimental challenges in conducting 3D3C measurements in the viscous sublayer and buffer layer are substantial. First, the seeding density that can be achieved is significantly lower when a 3D flow volume is captured using a V3V camera. Second, the accuracy in measuring a three-dimensional velocity field very close to the bed using methods such as 3D particle tracking must be established. It is intended that the 2D PIV measurements obtained in this study would provide a valuable data set for comparison with the 3D3C measurements. The measured data should also be useful for testing LES and other advanced Computational Fluid Dynamics (CFD) models of coherent structures in the bottom boundary layer of near-breaking waves.

Our longer-term goal is to measure the velocity field of the unsteady, three-dimensional turbulent boundary layer created by the impact of breaking-wave-generated vortices on the bottom and determine the distribution of instantaneous bed shear stress. Numerical models of coastal sediment transport often use the logarithmic law to compute the bed shear stress given the velocity at the first computational grid point in the outer layer. The existence of the law of the wall in vortex impingement is questionable but is a critical issue in numerical modeling of surf zone hydrodynamics and sediment transport. High quality boundary layer flow measurements will be essential for assessing whether the law of the wall can be applied under breaking waves and if not, for developing and validating more advanced wall functions for predicting the bed shear stress.

CRediT authorship contribution statement

Francis C.K. Ting: Conceptualization, Methodology, Formal analysis, Investigation, Data curation, Writing – original draft, Writing – review & editing, Visualization, Funding acquisition. **Gunnar S. Kern:** Investigation.

Declaration of competing interest

The authors declare the following financial interests/personal relationships which may be considered as potential competing interests: Francis Ting reports financial support was provided by National Science Foundation.

Data availability

Data will be made available on request.

Acknowledgements

This study was sponsored by the National Science Foundation (NSF) through Grant OCE-2049293. The support of NSF is gratefully acknowledged.

References

Acarlar, M.S., Smith, C.R., 1987. A study of hairpin vortices in a laminar boundary layer. Part 2. Hairpin vortices generated by fluid injection. J. Fluid Mech. 175, 43–83. https://doi.org/10.1017/S0022112087000284.

Akhavan, R., Kamm, R.D., Shaprio, A.H., 1991. An investigation of transition to turbulence in bounded oscillatory Stokes flows. Part 1. Experiments. J. Fluid Mech. 225, 395–422. https://doi.org/10.1017/S0022112091002100.

Allen, P.A., 1997. Earth Surface Processes. Wiley-Blackwell, p. 404.

Baldock, T.E., 2012. Discussion of Laboratory investigation of pressure gradients induced by plunging breakers, by Pedrozo-Acuña et al. Coast. Eng. 66, 1–2. https://doi.org/10.1016/j.coastaleng.2012.03.008.

Carstensen, S., Sumer, B.M., Fredsøe, J., 2010. Coherent structures in wave boundary layers. Part 1. Oscillatory motion. J. Fluid Mech. 646, 169–206. https://doi.org/10.1017/S0022112009992825.

Costamagna, P., Vittori, G., Blondeaux, P., 2003. Coherent structures in oscillatory boundary layers. J. Fluid Mech. 474, 1–33. https://doi.org/10.1017/S0022112002002665.

Cox, D.T., Kobayashi, N., 2000. Identification of intense, intermittent coherent motions under shoaling and breaking waves. J. Geophys. Res.:Oceans 105 (C6), 14223–14236. https://doi.org/10.1029/2000JC900048.

Goring, D.G., 1978. Tsunamis – The Propagation of Long Waves onto a Shelf. PhD Thesis. California Institute of Technology, Pasadena, p. 356.

Grass, A.J., 1971. Structural features of turbulent flow over smooth and rough boundaries. J. Fluid Mech. 50 (2), 233–255. https://doi.org/10.1017/S0022112071002556.

Hino, M., Kashiwayanagi, M., Nakayama, A., Hara, T., 1983. Experiments on the turbulent statistics and the structure of a reciprocating oscillatory flow. J. Fluid Mech. 131, 363–400. https://doi.org/10.1017/S0022112083001378.

Jensen, B.L., Sumer, B.M., Fredsøe, J., 1989. Turbulent oscillatory boundary layers at high Reynolds numbers. J. Fluid Mech. 206, 265–297. https://doi.org/10.1017/S0022112089002302.

Kiger, K., 2015. PIV Basics: Correlation. *SEDITRANS Summer School on Measurement Techniques for Turbulent Open-Channel Flows*. http://www.civil.ist.utl.pt/~ruif/SUMMER_SCHOOL/presentations/PIV_basics_correlation_final.pdf.

Kim, H.T., Kline, S.J., Reynolds, W.C., 1971. The production of turbulence near a smooth wall in a turbulent boundary layer. J. Fluid Mech. 50 (1), 133–160. https://doi.org/10.1017/S0022112071002490.

Kline, S.J., Reynolds, W.C., Schraub, F.A., Runstadler, P.W., 1967. The structure of turbulent boundary layers. J. Fluid Mech. 30 (4), 741–773. https://doi.org/10.1017/S0022112067001740.

Larsson, J., Kawai, S., Bodart, J., Bermejo-Moreno, I., 2015. Large eddy simulation with modeled wall-stress: recent progress and future directions. Mechanical Engineering Reviews 3 (1), 15–00418. https://doi.org/10.1299/mer.15-00418.

Lin, C., Huang, H.-H., 2002. Observation and measurement of the bottom boundary layer flow in the prebreaking zone of shoaling waves. Ocean. Eng. 29 (12), 1479–1502. https://doi.org/10.1016/S0029-8018(01)00094-4.

Lin, C., Yeh, P.-H., Kao, M.-J., Yu, M.-H., Hsieh, S.-C., Chang, S.-C., Wu, T.-R., Tsai, C.-P., 2015b. Velocity fields in near-bottom and boundary layer flows in pre-breaking zone of solitary wave propagating over a 1:10 slope. J. Waterw. Port, Coast. Ocean Eng. 141 (3). https://doi.org/10.1061/(ASCE)WW.1943-5460.0000269.

Lin, C., Yu, S.-M., Yeh, P.-H., Yu, M.-H., Tsai, C.-P., Hsieh, S.-C., Kao, M.-J., Tzeng, G.-W., Raikar, R., 2015a. Characteristics of boundary layer flow induced by solitary wave propagating over horizontal bottom. J. Mar. Sci. Technol. 23 (6), 909–922. https://doi.org/10.6119/JMST-015-0610-9.

Liu, P.L.-F., Park, Y.S., Cowen, E.A., 2007. Boundary layer flow and bed shear stress under a solitary wave. J. Fluid Mech. 574, 449–463. https://doi.org/10.1017/S0022112006004253.

Mason, P.J., Callen, N.S., 1986. On the magnitude of the subgrid-scale eddy coefficient in large-eddy simulations of turbulent channel flow. J. Fluid Mech. 162, 439–462. https://doi.org/10.1017/S0022112086002112.

Mazzuoli, M., Vittori, G., Blondeaux, P., 2011. Turbulent spots in oscillatory boundary layers. J. Fluid Mech. 685, 365–376. https://doi.org/10.1017/jfm.2011.320.

Mier, J.M., Fytanidis, D.K., Garcia, M.H., 2021. Mean flow structure and velocity–bed shear stress maxima phase difference in smooth wall, transitionally turbulent oscillatory boundary layers: experimental observations. J. Fluid Mech. 922, A29. https://doi.org/10.1017/jfm.2021.510.

Nakagawa, H., Nezu, I., 1981. Structure of space-time correlations of bursting phenomena in an open-channel flow. J. Fluid Mech. 104, 1–43. https://doi.org/10.1017/S0022112081002796.

Nezu, I., 1977. Turbulent structure in open-channel flows. PhD Thesis. Kyoto University, Kyoto, Japan.

Nezu, I., Nakagawa, H., 1993. Turbulence in Open-Channel Flows. A. A. Balkema, p. 281.

Offen, G.R., Kline, S.J., 1974. Combined dye-streak and hydrogen-bubble visual observations of a turbulent boundary layer. J. Fluid Mech. 62 (2), 223–239. https://doi.org/10.1017/S0022112074000656.

Offen, G.R., Kline, S.J., 1975. A proposed model of the bursting process in turbulent boundary layers. J. Fluid Mech. 70 (2), 209–228. https://doi.org/10.1017/S002211207500198X.

Panton, R.L., 1984. Incompressible Flow. John Wiley and Sons, p. 780.

Panton, R.L., 2001. Overview of the self-sustaining mechanisms of wall turbulence. Prog. Aero. Sci. 37 (4), 341–383. https://doi.org/10.1016/S0376-0421(01)00009-4.

Piomelli, U., Balaras, E., 2002. Wall-layer models for large-eddy simulations. Annu. Rev. Fluid Mech. 34 (1), 349–374. https://doi.org/10.1146/annurev.fluid.34.082901.144919.

Pope, S.B., 2000. Turbulent Flows. Cambridge University Press, p. 802.

Pujara, N., Liu, P.L.-F., 2014. Direct measurements of local bed shear stress in the presence of pressure gradients. Exp. Fluids 55, 1767. https://doi.org/10.1007/s00348-014-1767-8.

Raffel, M., Willert, C., Kompenhans, J., 1998. Particle Image Velocimetry: A Practical Guide. Springer-Verlag, Berlin, p. 253.

Robinson, S.K., 1991. Coherent motions in the turbulent boundary layer. Annu. Rev. Fluid Mech. 23, 601–639. https://doi.org/10.1146/annurev.fl.23.010191.003125.

Scandura, P., Faraci, C., Foti, E., 2016. A numerical investigation of acceleration-skewed oscillatory flows. J. Fluid Mech. 808, 576–613. https://doi.org/10.1017/jfm.2016.641.

Seelam, J.K., Guard, P.A., Baldock, T.E., 2011. Measurement and modeling of bed shear stress under solitary waves. Coast. Eng. 58 (9), 937–947. https://doi.org/10.1016/j.coastaleng.2011.05.012.

Smith, C.R., 1984. A synthesized model of near-wall behavior in turbulent boundary layers. In: Proc. of 8th Symposium on Turbulence. University of Missouri-Rolla, pp. 299–327.

Smith, C.R., 1996. Coherent flow structures in smooth-wall turbulent boundary layers: facts, mechanics and speculation. In: Ashworth, P.J., Bennett, S.J., Best, J.L., McLelland, S.J. (Eds.), Coherent Flow Structures in Open Channels. John Wiley & Sons, p. 760.

Spalding, D.B., 1961. A single formula for the law of the wall. J. Appl. Mech. 28 (3), 455–458. https://doi.org/10.1115/1.3641728.

Sumer, B.M., Jensen, P.M., Sørensen, L.B., Fredsøe, J., Liu, P.L.-F., Carstensen, S., 2010. Coherent structures in wave boundary layers. Part 2. Solitary motion. J. Fluid Mech. 646, 207–231. https://doi.org/10.1017/S0022112009992837.

Sumer, B.M., Sen, M.B., Karagali, I., Ceren, B., Fredsøe, J., Sottile, M., Zilioli, L., Fuhrman, D.R., 2011. Flow and sediment transport induced by a plunging solitary wave. J. Geophys. Res.: Oceans 116 (C1). https://doi.org/10.1029/2010JC006435.

Tennekes, H.T., Lumley, J.L., 1989. A First Course in Turbulence. 12th Printing. The MIT Press, p. 300.

Ting, F.C.K., 2006. Large-scale turbulence under a solitary wave. Coast. Eng. 53 (5–6), 441–462. https://doi.org/10.1016/j.coastaleng.2005.11.004.

Ting, F.C.K., Reimnitz, J., 2015. Volumetric velocity measurements of turbulent coherent structures induced by plunging regular waves. Coast. Eng. 104, 93–112. https://doi.org/10.1016/j.coastaleng.2015.07.002.

van der A, D.A., O'Donoghue, T., Davies, A.G., Ribberink, J.S., 2011. Experimental study of the turbulent boundary layer in acceleration-skewed oscillatory flow. J. Fluid Mech. 684, 251–283. https://doi.org/10.1017/jfm.2011.300.

van der A, D.A., Scandura, P., O'Donoghue, T., 2018. Turbulence statistics in smooth wall oscillatory boundary layer flow. J. Fluid Mech. 849, 192–230. https://doi.org/10.1017/jfm.2018.403.

Vittori, G., Verzicco, R., 1998. Direct simulation of transition in an oscillatory boundary layer. J. Fluid Mech. 371, 207–232. https://doi.org/10.1017/S002211209800216X.

Vittori, G., Blondeaux, P., 2008. Turbulent boundary layer under a solitary wave. J. Fluid Mech. 615, 433–443. https://doi.org/10.1017/S0022112008003893.

Zhou, Z., Hsu, T.-J., Cox, D., Liu, X., 2017. Large-eddy simulation of wave-breaking induced turbulent coherent structures and suspended sediment transport on a barred beach. J. Geophys. Res.:Oceans 122 (1), 207–235. https://doi.org/10.1002/2016JC011884.

Zhou, Z., Sangermano, J., Hsu, T.-J., Ting, F.C.K., 2014. A numerical investigation of wave-breaking-induced turbulent coherent structure under a solitary wave. J. Geophys. Res.:Oceans 119 (10), 6952–6973. https://doi.org/10.1002/2014JC009854.